Applied Catalysis B: Environmental 340 (2024) 123201

Contents lists available at ScienceDirect

Applied Catalysis B: Environmental

journal homepage: www.elsevier.com/locate/apcatb

Synthesis of *n*-butanol-rich C_{3+} alcohols by direct CO_2 hydrogenation over a stable Cu–Co tandem catalyst

Muhammad Irshad [a,1], Hee-Joon Chun [b,1], Muhammad Kashif Khan [a,c], Heuntae Jo [c], Seok Ki Kim [d,e,*], Jaehoon Kim [a,c,f,**]

[a] School of Chemical Engineering, Sungkyunkwan University, 2066, Seobu-Ro, Jangan-Gu, Suwon, Gyeong Gi-Do 16419, Republic of Korea
[b] Corporate R&D Institute, Samsung Electro-Mechanics Co., Ltd., 150, Maeyoung-ro, Yeongtong-gu, Suwon, Gyeonggi-do 16674, Republic of Korea
[c] School of Mechanical Engineering, Sungkyunkwan University, 2066, Seobu-Ro, Jangan-Gu, Suwon, Gyeong Gi-Do 16419, Republic of Korea
[d] Department of Energy System Research, Ajou University, Suwon 16499, Republic of Korea
[e] Department of Chemical Engineering, Ajou University, Suwon 16499, Republic of Korea
[f] SKKU Advanced Institute of Nano Technology, 2066, Seobu-Ro, Jangan-Gu, Suwon, Gyeong Gi-Do 16419, Republic of Korea

ARTICLE INFO

Keywords:
Butanol
C_3 +alcohols
Copper
Cobalt
Catalyst stability
CO_2 conversion

ABSTRACT

The direct conversion of CO_2 into liquid fuels and chemical heterogeneous catalysts is considered a promising route to mitigate global warming issues. However, the production of *n*-butanol-rich C_{3+} alcohol from CO_2 remains a significant challenge. Herein, we demonstrate that a Cu-rich bimetallic Cu–Co catalyst can achieve an unprecedentedly high space-time yield (STY_{C3+OH}) of 80.8 mg g^{-1} h^{-1}. The decoration of Co nanoparticles onto the dendritic Cu substrate established a crucial balance between CH_x and CH_3O* and regulated C–C coupling, which is a prerequisite for C_{3+} alcohol synthesis. We provide new mechanistic insights into *n*-butanol synthesis involving the C–O bond dissociation of an acetaldehyde intermediate on the interfacial Cu–Co site and subsequent C–C bond formation on the Cu site. Furthermore, the Cu–Co catalyst exhibited exceptional stability up to 1000 h by effectively suppressing re-oxidation and carbon deposition. The Cu–Co catalyst has great potential for large-scale CO_2 hydrogenation to C_{3+} alcohol owing to its high selectivity and remarkable stability.

1. Introduction

The rapid increase in anthropogenic CO_2 emissions over the past decades because of the overuse of fossil fuels poses a serious, irreversible threat to the global ecosystem [1,2]. The direct use of CO_2 as a feedstock to produce fuels and chemicals is one of the most promising approaches to mitigate CO_2 emissions [3]. Thermocatalytic CO_2 hydrogenation is an effective technique to produce a variety of fuels and chemicals, including C_{5+} paraffins [4], gasoline [5], lower olefins [6], long-chain α-olefins [7], aromatics [8], carboxylic acids [9], and alcohols [10,11]. Among these products, higher alcohols, specifically C_{3+} alcohols ($C_{3+}OH$), deserve considerable attention owing to their widespread applications and enormous market demand in both the transportation and chemical sectors. *n*-Propanol, for instance, is used as both a solvent and intermediate in the chemical, medical, and cosmetic industries. *n*-Butanol is used to produce vanishes, plastics, lubricants, and synthetic rubbers; it is also used as a cleaning solvent and as an additive in the food and cosmetics industries. Short-chain C_3–C_4 alcohols can be used as gasoline with high energy density, water tolerance, and octane number [12], whereas long-chain C_{5+} alcohols are mainly used as surfactants and chemical intermediates. To date, the commercial production routes of *n*-propanol and *n*-butanol are based on the hydroformylation of ethylene and propylene, respectively, which are produced from the naphtha cracking of crude oil [13,14]. An alternative pathway for the demonstration-scale synthesis of *n*-butanol based on the fermentation of renewable carbohydrates has been developed [12]; however, the microbial production of *n*-propanol remains a considerable challenge [15]. Long-chain C_{5+} alcohols are produced by the hydration of alkenes originating from petroleum [16]. Thus, the production of $C_{3+}OH$ from direct CO_2 hydrogenation can pave the way to sustainable chemical and

* Corresponding author at: Department of Energy System Research, Ajou University, Suwon 16499, Republic of Korea.
** Correspondence to: School of Mechanical Engineering, School of Chemical Engineering, and SKKU Advanced Institute of Nano Technology, Sungkyunkwan University, 2066, Seobu-Ro, Jangan-Gu, Suwon, Gyeong Gi-Do 16419, Republic of Korea.
E-mail addresses: seokki@ajou.ac.kr (S.K. Kim), jaehoonkim@skku.edu (J. Kim).
[1] These authors contributed equally to this study.

https://doi.org/10.1016/j.apcatb.2023.123201
Received 16 June 2023; Received in revised form 7 August 2023; Accepted 21 August 2023
Available online 26 August 2023
0926-3373/© 2023 Elsevier B.V. All rights reserved.

energy sources by reducing the dependency on fossil resources to address climate change.

CO_2-to-methanol (C_1OH) conversion is a well-established route [17], and its commercial-scale production was realized in early 2010 [18]. Numerous catalysts have been developed for CO_2-to-ethanol conversion, as discussed in recent literature [10,11]. However, the direct conversion of CO_2 to $C_{3+}OH$ is still technically difficult (Table S1). Specifically, the space-time-yields of $C_{3+}OH$ (STY_{C3+OH}) are low (1.2–21.0 mg g_{cat}^{-1} h^{-1}), with the long-term stability of the available catalysts over 1000 h yet to be verified; these properties are highly critical for the legitimate industrial implementation of direct CO_2 conversion to obtain higher alcohols. The technological hurdles in the synthesis of C_{3+} alcohols are as follows: (1) The product distribution during alcohol synthesis is governed by the Anderson–Schulz–Flory (ASF) distribution, which limits the chain growth required for the synthesis of $C_{3+}OH$ [19]; (2) The reverse-water–gas-shift (RWGS) reaction for CO production and insertion of CO into the growing CH_x chain obtained via Fischer–Trosph synthesis (FTS) should occur simultaneously (thus, two active sites must be present in proximity) [20]; (3) Because of the inherent complexity and multistep reactions required for $C_{3+}OH$ synthesis, numerous side reactions can occur, leading to a decrease in $C_{3+}OH$ selectivity; and (4) Mechanistic insights into the formation of higher alcohols have not been obtained, although a widely accepted CO-mediated mechanism is believed to be involved in the synthesis of C_{3+} alcohols [21]. For instance, the mechanism of the direct dissociation of CO or C−O cleavage of the methoxy (CH_3O^*) intermediate to produce ethanol from CO_2 hydrogenation has been debated [22,23].

Herein, we demonstrate that $C_{3+}OH$ can be produced in high yield by the direct hydrogenation of CO_2 over a novel Na-promoted bimetallic CuCo catalyst (Na–CuCo-*y*). The rationale behind the design of a single bimetallic catalyst with metallic Cu and Co phases is as follows: the metallic Co site actively participates in the dissociation of CO and FTS under mild conditions [24], while Cu produces alcoholic species by inserting CO into the growing chains that occur in its vicinity [25]. This study explores a strategy to suppress the activity of Co toward methanation to achieve adequate C–C coupling and tailor the kinetics for balanced CO/CH_x adsorption, thereby boosting $C_{3+}OH$ production. The optimized Na–CuCo catalyst exhibits a high $C_{3+}OH/ROH$ fraction of 73.5%, with an overall selectivity of alcohols in the liquid product stream of 58% at a CO_2 conversion rate of 22.1%, resulting in an unprecedented STY_{C3+OH} of 80.8 mg g_{cat}^{-1} h^{-1} (Table S1, Fig. S1). Indeed, the $C_{3+}OH$ yield obtained through this catalyst is the highest reported to date. CO_2 conversion and $C_{3+}OH$ selectivity were maintained for up to 1000 h, rendering our strategy very promising for practical applications. Among the $C_{3+}OH$ products formed, *n*-butanol was the major product (STY = 34.1 mg g_{cat}^{-1} h^{-1}), and its reaction pathway was explored. In the following sections, the tuning of the activity of the Na–CuCo catalyst for $C_{3+}OH$ production, optimization of the process parameters, characterization of the catalyst, and reaction mechanisms are investigated using in situ and ex situ techniques, and theoretical studies are performed using computational analysis.

2. Experimental section

2.1. Catalyst preparation

A series of Na-promoted Cu–Co bimetallic oxide (Na–CuCo-*y*) catalysts with varying Cu contents ($y = Cu/(Cu+Co) \times 10$) were synthesized via a simple coprecipitation method. Nitrate salts of both metals were used as precursors. As a typical example, the representative Na–CuCo-9 catalyst was synthesized as follows. Known amounts of copper(II) nitrate hemihydrate ($Cu(NO_3)_2{\cdot}2.5\ H_2O$, 98.0%, Alfa Aesar, USA) and cobalt(II) nitrate hexahydrate ($Co(NO_3)_2{\cdot}6\ H_2O$, 99.9%, Sigma Aldrich, USA) were dissolved in 100 mL of distilled and deionized (DDI) water to prepare 1 M solutions. An equal volume of 2 M sodium carbonate (Na_2CO_3, 99.98%, Sigma Aldrich) solution dissolved using DDI water was prepared as a precipitant. The aqueous Na_2CO_3 solution was added dropwise to the copper(II) nitrate and cobalt(II) nitrate solutions under stirring at 80 °C, leading to the emergence of a light-green precipitate. The pH of the solution was adjusted to 8–9 via the dropwise addition of dilute HCl. The mixture was continuously stirred for 12 h using a magnetic bar and then aged for 12 h at 23 ± 2 °C. The precipitate was filtered using Whatman #2 filter paper and washed with 300 mL of DDI water. The filter cake collected after washing was placed in a drying oven at 80 °C for 12 h. Finally, the catalyst was calcined at 600 °C by increasing the temperature at a Ramp rate of 1.5 °C min^{-1} for 6 h under static air conditions.

2.2. Catalyst performance evaluation

The CO_2 conversion performance of the catalysts was evaluated in a continuous stainless-steel fixed-bed reactor. Details of the reactor design and reaction setups can be found in our previous study [7]. In a typical experiment, 1 g of the catalyst was diluted with 3 mL of silica (Fisher Chemicals, S/0365/60) and then charged into the reactor. Prior to CO_2 hydrogenation, the Na–CuCo-*y* catalyst was activated by reduction at 350 °C and 4.0 MPa using H_2 flowing at a rate of 50 mL min^{-1} for 12 h. After catalyst reduction, the reactor was allowed to cool to 330 °C. A mixture of CO_2 (1000 mL g^{-1} h^{-1}) and H_2 (1000 mL g^{-1} h^{-1}) was introduced into the reactor at a fixed pressure of 4.0 MPa. As CO_2 hydrogenation began, the product stream was passed through a condenser, the temperature of which was maintained at 4 °C to liquefy the resultant alcohols, oxygenated species, and C_{5+} hydrocarbons. Details of the experimental procedures used to analyze and quantify the unreacted CO_2, gaseous products, and liquid products via online refinery gas analysis–gas chromatography (RGA–GC[26]), gas chromatography–time-of-flight mass spectrometry (GC–TOF/MS[27]), high-performance liquid chromatography (HPLC), and gas chromatography–flame ionization detection (GC–FID) are available in our recent study [4]. Quantification of the liquid products was performed using the effective carbon number (ECN) method by constructing the calibration curves of standard compounds (*n*-butanol and *n*-decane).

The distribution of all gaseous and liquid species obtained over the tested catalysts was expressed as carbon mole% (C-mol%). CO_2 conversion, $C_{3+}OH$, hydrocarbon, and CO selectivity, and $C_{3+}OH$ yield were calculated using Eqs. 1–5. The carbon balance of the products was calculated using Eq. 6.

$$CO_2\text{conversion}(C-\text{mol}\%) = \frac{CO_{2in}-CO_{2out}}{CO_{2in}} \times 100\% \quad (1)$$

$$\text{CO selectivity}(C-\text{mol}\%) = \frac{CO_{out}}{CO_{2in}-CO_{2out}} \times 100\% \quad (2)$$

$$C_{3+}OH\ \text{selectivity}(C-\text{mol}\%)\text{excluding CO} = \frac{\text{Moles of}\ C_i\quad \text{alcohol} \times i}{CO_{2in}-CO_{2out}} \times 100\% \quad (3)$$

$$C_{3+}OH\,\text{yield}(C-\text{mol}\%) = \frac{\text{Selectivity of}\,C_{3+}OH\,\text{including CO} \times CO_2\text{conversion}}{100} \quad (4)$$

$$\text{Hydrocarbon selectivity}(C-\text{mol}\%)\text{excluding CO} = \frac{\text{Moles of}\ C_i\quad \text{hydrocarbon} \times i}{CO_{2in}-CO_{2out}} \times 100\% \quad (5)$$

$$\text{Carbon balance} = \frac{CO_{out} + \sum_{i=1}^{n=5} RGA - GC, C_iH_j + \sum_{i=1}^{n=5} HPLC, C_iH_jO_k \quad + \sum_{i=6}^{n=19} GC - FID, C_iH_j}{CO_{2in} - CO_{2out}} \tag{6}$$

where the molar fraction of CO_2 in the reactants, unreacted CO_2 in the effluent, and CO in the gaseous products are expressed as $CO_{2\ in}$, $CO_{2\ out}$, and CO_{out}, respectively.

2.3. Catalyst characterization

The crystallinity and phase transformation of the calcined, reduced, and spent Na–CuCo-*y* catalysts were analyzed using a Rigaku X-ray diffractometer (XRD; D/Max–2500 V/PC, Japan) with Ni-filtered Cu–Kα radiation ($\lambda = 1.5418$ Å, 50 mA, 40 kV). All catalysts were scanned over the 2θ range of 5–90° with a scan step of 0.02° and scan rate of 2 ° min^{-1}. A field-emission scanning electron microscope (FE-SEM; S-4100, Hitachi, Japan) and Cs-corrected scanning transmission electron microscope (STEM; TitanTM 80–300, FEI, USA) equipped with a fast CCD camera (Gatan, Oneview 1095) were used to determine the morphology and particle size distribution of the catalysts. The microstructure and elemental mappings of the catalysts were examined using a high-resolution transmission electron microscope (HR-TEM; FEI Talos F200X, USA) fitted with an energy-dispersive X-ray spectrometer (EDX; Super-X EDX, Bruker, USA) operated at 200 keV. A Belsorp-mini II instrument (BEL Inc., Japan) was used to acquire the N_2 adsorption–desorption profiles of the catalysts at −196 °C, thereby enabling the observation of their textural characteristics. The multipoint Brunauer–Emmett–Teller (BET) method was used to measure the specific surface areas of the catalysts, and Barrett–Joyner–Halenda (BJH) plots were used to characterize their pore size distributions. Absorbed moisture was removed prior to the N_2 adsorption–desorption analysis by pretreatment under vacuum at 120 °C for 12 h. The amounts of metallic species (Cu, Co, and Na) in the calcined, reduced, and spent catalysts were determined using inductively coupled plasma optical emission spectrometry (ICP-OES; Optima 7300 V, PerkinElmer, USA).

Cu K-edge and Co K-edge X-ray absorption spectroscopy (XAS) was conducted in transmission mode at the 8 C beamline of the Pohang Accelerator Laboratory using a Si(111) double-crystal monochromator. The reference spectra of Cu and Co foils were collected simultaneously with the spectra of the catalysts for energy calibration. Athena/Artemis software was used to process the data for X-ray absorption near edge structure (XANES) and extended X-ray absorption fine structure (EXAFS) analyses [28]. The extracted EXAFS signals χ(k) were weighted by a k^3 factor to emphasize high-energy oscillations. Fourier transform was carried out in the *k*-range of 3.0–11.0 Å using a Hanning window function to obtain the magnitude plot of the EXAFS spectra in the R-space. The X-ray photoelectron spectroscopy (XPS) scans were attained using a Thermo Scientific (model: ESCALAB250Xi, UK) spectrometer with reference of the C–C bond assigned a bonding energy (BE) of 284.8 eV.

A BELCAT-M instrument (BET Inc., Japan) equipped with a thermal conductivity detector (TCD) and quadrupole mass spectrometer (QMS; Transpector® CPM 3, Inficon Inc., USA) fitted with a residual gas analyzer was used to perform the temperature-programmed reduction (TPR) experiments. Prior to TPR analysis, the catalyst sample was pretreated at 200 °C in ultra-high purity Ar gas (99.999%, JC Gas Company, South Korea) flowing at a rate of 40 mL min^{-1}. The temperature gradually increased at a rate of 10 °C min^{-1} and then maintained for 2 h to remove all moisture and absorbed impurities. After the pretreatment, the temperature was decreased to 50 °C by natural cooling. A gas mixture of 5% H_2 in Ar was then introduced into the TPR cell at a flow rate of 40 mL min^{-1} for H_2-TPR analysis; 10% CO in Ar was introduced at a flow rate of 40 mL min^{-1} for CO-TPR analysis. Finally, TCD signals were recorded as the temperature was increased from 50 to 800 °C at a heating rate of 5 °C min^{-1}.

Temperature-programmed oxidation (TPO) of the spent Na–CuCo-9 catalyst collected after a 1000 h-on-stream reaction was conducted in the same instrument used for the TPR experiments. Prior to TPO analysis, the catalyst sample was pretreated at 150 °C slightly in Ar gas (99.999%) flowing at a rate of 50 mL min^{-1}. The temperature gradually increased at a rate of 10 °C min^{-1} and then maintained for 2 h to remove all moisture and absorbed impurities. After the pretreatment, the temperature was decreased to 50 °C by natural cooling. Pure O_2 (99.995% purity, JC Gas Company) was introduced into the cell at a flow rate of 50 mL min^{-1}, and the temperature was increased from 50 to 900 °C at a rate of 10 °C min^{-1}. The effluent was directed toward the QMS apparatus to enable the identification of CO_2 and other gaseous species liberated from the catalyst surface during oxidation.

Temperature-programmed surface reaction (TPSR) analysis was conducted over the Na–CuCo-9 catalyst. A catalyst sample weighing 50 mg was dosed in a sample tube. The temperature was increased to 350 °C at a rate of 10 °C min^{-1} and maintained for 2 h first under pure He (99.999%, JC Gas Company) as a carrier gas flowing at a rate of 50 mL min^{-1} and then under 5% H_2/Ar as a reducing gas flowing at a rate of 50 mL min^{-1}. The system was flushed with ultra-high-purity He at a flow rate of 50 mL min^{-1} for 30 min. After the pretreatment, the temperature was decreased to 50 °C by natural cooling. A continuous flow of mixed CO/He (5% CO/He, JC Gas Company) was injected into the sample tube at a flow rate of 30 mL min^{-1} for 1 h to completely saturate the catalyst with CO. Physically absorbed CO gas was removed by flushing the system with ultra-high-purity He at a flow rate of 50 mL min^{-1} for 30 min. Finally, TCD and QMS signals were recorded as the tube temperature was increased from 50° to 800 °C at a heating rate of 10 °C min^{-1} under 5% H_2/Ar gas flowing at a rate of 50 mL min^{-1} to detect the CO and CH_4 gases desorbed from the catalyst surface.

Near-ambient pressure XPS (NAP-XPS) analysis was carried out using the atmospheric-pressure XPS (AP-XPS) system of a SPEC Surface Nano Analysis apparatus (SPECS, GmbH, Germany) installed at beamline 8A2 of the Pohang Accelerator Laboratory (Pohang, South Korea) [29]. The AP-XPS system consisted of two chambers: an analytical chamber and a sample load-lock. The analytical chamber was armed with a PHOIBOS hemispherical electron analyzer and a micro-focused source that emitted AlKα X-rays with a beam size of 300 μm. High-purity Ar, CO_2, and H_2 gas were charged into the analytical chamber at a partial pressure of 100 Pa each, and the NAP-XPS data were recorded at a temperature of 330 °C. The SpecsLab Prodigy program was used to record and analyze the C 1 s, O 1 s, Cu 2p, and Co 2p spectra in situ. An ESCALAB250Xi (Thermo Scientific, UK) spectrometer was used for the ultra-high-vacuum XPS (UHV-XPS) analyses of the catalysts. All peak assignments in the recorded spectra were referenced to the C–C bond at 284.8 eV.

The reaction intermediates produced during CO_2 hydrogenation were investigated using diffuse reflectance infrared Fourier transform (DRIFT) spectroscopy. DRIFT analysis was performed using a Perkin Elmer Frontier spectrometer fitted with a Harrick Praying Mantis cell (USA) and a mercury cadmium telluride (MCT) detector. The weight ratio of the catalyst sample to KBr was kept at 5:95. All reduced catalysts collected from the fixed-bed reactor were in situ activated in the DRIFT cell at 300 °C and 3.0 MPa under pure H_2 flowing at a rate of 50 mL min^{-1} for 6 h. The cell was then cooled to 50 ± 2 °C, and the background spectra were collected. CO_2 DRIFT analysis was performed in the same apparatus by flowing CO_2 (99.995%) at a rate of

16.7 mL min^{-1} at pressures ranging from 0.1 to 3.0 MPa. A back-pressure regulator was used to control the pressure of the DRIFT cell (26–2300 Series, Tescom, USA). IR spectra were collected as the temperature was ramped from 50 to 300 °C at a rate of 2.5 °C min^{-1}. Approximately 30 min after a steady state was achieved at 300 °C, the CO_2 gas was switched to H_2 gas (flow rate of 50 mL min^{-1} at 300 °C and 3.0 MPa), and the IR spectra for CO_2 hydrogenation were recorded for 3 h. For in situ reaction, following the in situ reduction of the catalysts, CO_2 and H_2 (H_2/CO_2 ratio of 1:1) were injected into the DRIFT cell to observe the CO_2 hydrogenation behavior under actual reaction conditions. DRIFT analysis was carried out over the Na–CuCo-9 catalyst at varying pressures of 0.1–3.0 MPa at 50 °C andtemperatures of 50–300 °C at 3.0 MPa to understand the effects of temperature and pressure on CO_2 hydrogenation.

In situ DRIFT spectra were collected during hydrogenation using the methanol, ethanol, and acetaldehyde probe reactions over the Na–CuCo-9 catalyst. The catalyst was activated by ramping the temperature to 350 °C at a rate of 5 °C min^{-1} and 3.0 MPa with H_2 flowing at a rate of 50 mL min^{-1} for 8 h, followed by purging with N_2 for 2 h. The DRIFT cell was subsequently cooled to 50 °C. Adsorption of the probe molecule was performed at 50 °C with a N_2 + standard vapor flow rate of 16.7 mL min^{-1} for 1 h. Finally, hydrogenation of the probe molecule was performed by increasing the temperature from 50 to 330 °C at a ramp rate of 5 °C min^{-1} under a H_2 flow rate of 20 mL min^{-1}.

2.4. Computational methods

All density functional theory (DFT) geometric optimizations and energy calculations were carried out using the Vienna Ab initio Simulation Package (VASP) code [30,31]. Interactions between valence and core electrons were described using the projector-augmented wave (PAW) approach, and long-range dispersion was corrected via the Grimme method (DFT-D_2) [32]. A 400 eV cut-off energy was used for the plane-wave basis set. The convergence criteria for energy and atomic force were set to 10^{-4} eV and 10^{-4} eV $Å^{-1}$, respectively.

A (1 × 5) Cu(211) slab was obtained by cleaving bulk Cu (cubic phase, space group: *Fm-3 m*) with lattice parameters of $a = b = c = 3.64$ Å [33]. The unit cell featured four layers perpendicular to the terrace plane, among which the bottom two were frozen. The Co-added Cu bimetallic catalysts were modeled by replacing Cu atoms located at the step edge of Cu(211) with Co, as depicted in a previous study [34]. This model is in line with our experimental Co–Cu catalysts bearing Cu-rich and Co-segregated surfaces. Our surface models were denoted as Cu(211)-*n*Co, where *n* refers to the total number of Co atoms at the step edge of the Cu(211) unit cell ($n = 0, 1, 3, 5$). The images of all slabs are given in Fig. S28. During geometry optimization, the Brillouin zone was sampled using Monkhorst-Pack *k*-point grids of 4 × 2 × 1. A 15 Å vacuum gap was introduced perpendicular to the surface to prevent interactions between slabs.

The Gibbs free energy (G) of the elementary steps for butanol formation at a given temperature (T) is defined as:

$$\Delta G = \Delta E_{DFT} + \Delta ZPE - T\Delta S \quad , \tag{7}$$

where ΔE_{DFT}, ΔZPE, and ΔS are the changes in DFT energy, zero-point energy, and entropy, respectively. The chemical potentials (μ) for gaseous CO_2, H_2, and H_2O were calculated as:

$$\mu_{gas} = E_{gas} + ZPE_{gas} + \Delta H_{gas}{}^{o} - TS_{gas}{}^{o} + k_B T \ln\left(\frac{P}{P^o}\right), \tag{8}$$

where E_{gas}, ZPE_{gas}, $\Delta H_{gas}{}^{o}$, $S_{gas}{}^{o}$, and P are the DFT energy, zero-point energy, standard enthalpy change from 0 to T, standard entropy at T, and pressure of gas-phase molecules, respectively. k_B and P^o refer to the Boltzmann constant and standard pressure (1 atm), respectively. The chemical potential for the reaction intermediate on the catalyst surface (X^*) is:

$$\mu_{X^*} = E_{X^*} + ZPE_{X^*} + \Delta U^o - TS^o, \tag{9}$$

where E_{X^*}, ZPE_{X^*}, ΔU^o, and S^o are the DFT energy, zero-point energy, standard internal energy change from 0 to T, and standard entropy of the reaction intermediate, respectively. The standard enthalpy and entropy for gas-phase species were calculated using the Shomate equation, the parameters of which are provided in the NIST WebBook [35]. The standard internal energy and entropy for surface reaction intermediates were estimated according to a harmonic approximation [36]. The minimum energy pathway for elementary reaction steps was computed using the climbing-image nudged elastic band (CI-NEB) method [36].

3. Results and discussion

3.1. CO_2 hydrogenation performance

CO_2 conversion over the Na-promoted bimetallic Na–CuCo-*y* catalysts with varying Cu contents ($y = Cu/(Cu+Co) \times 10$, Table S2) was evaluated, and the results are shown in Fig. 1A. The Cu-rich Na–CuCo-9 catalyst exhibited high selectivity toward $C_{3+}OH$ (27.4%), with a CO_2 conversion rate of 22.1%. Compared with the monometallic Na–Cu catalyst, the bimetallic Na–CuCo-*y* catalysts demonstrated drastic decreases in CO and C_1OH selectivity from 52.5% to 1.9% and from 50.0% to 20.0%, respectively. Compared with that over the monometallic Na–Co catalyst, CH_4 selectivity was significantly suppressed from 76.0% to 18.0% over the Na–CuCo-9 catalyst. When the Cu content in the Na–CuCo-5 catalyst was decreased to 50%, the formation of $C_{3+}OH$ gradually decreased, whereas the formation of CH_4 and paraffin-rich C_{5+} species increased. The rapid increase in CH_4 as the Co content increased to 90% indicates the dominance of chain termination in the reaction. Over the Na–CuCo-9 catalyst, the $C_{3+}OH$ yield (including CO) was 4.2% and the STY_{C3+OH} was 80.8 mg g_{cat}^{-1} h^{-1}; these values are much higher than those obtained from previously reported catalysts (0.1–3.0% and 1.2–21.0 mg g_{cat}^{-1} h^{-1}, respectively, Fig. 1B). A clear deviation from the ASF distribution was observed among the produced terminal alcohols (Fig. 1C): C_1OH (6.7%) < C_2OH (20.2%) < $C_{3+}OH$ (73.1%), in which *n*-butanol was the dominant product (42.7% of $C_{3+}OH$).

The long-term stability of the Na–CuCo-9 catalyst is illustrated in Fig. 1D. Following a slight decrease in CO_2 conversion and $C_{3+}OH$ selectivity during the initial 125 h of on-stream reaction, these properties were well maintained at ~20 and ~22%, respectively, by the end of the 1000 h-on-stream reaction. The exceptionally high stability of the Na–CuCo-9 catalyst indicates good resistance toward catalyst deactivation by, for example, carbon deposition, changes in the electronic states of active sites, and sintering, rendering it an excellent candidate for the practical-scale production of $C_{3+}OH$.

Process parameters including temperature, pressure, H_2/CO_2 ratio, and gas hourly space velocity (GHSV) were varied to optimize $C_{3+}OH$ selectivity over the Na–CuCo-9 catalyst. As the reaction temperature increased from 300° to 330°C, CO_2 conversion and $C_{3+}OH$ selectivity increased from 10.8% to 22.1% and from 8.3% to 27.4%, respectively, whereas CO and CH_4 selectivity decreased from 48.5% to 20.5% and from 50.5% to 18.0%, respectively (Fig. S2A). Further increases in temperature to 350 °C led to a rapid decrease in $C_{3+}OH$ selectivity to 4.1%, with CH_4 and saturated C_{2+} hydrocarbons being the main products at high temperatures. Thus, the incorporation of CO, CH_x formation and controlled growth of C–C chains, which are prerequisites for $C_{3+}OH$ synthesis, were well balanced at a moderate temperature of 330 °C owing to the combined hydrogenation activity of CO.

Because of the drastic cutback in the volume of gaseous reactants to produce liquid products, a high reaction pressure was favorable in increasing CO_2 conversion and liquid selectivity (Fig. S2B). At ambient pressure, CO_2 conversion was very low (9.1%), and gaseous C1 species (CO and CH_4) were obtained as major products. When the pressure was increased to 4.0 MPa, the selectivity of the CO_2 hydrogenation reaction

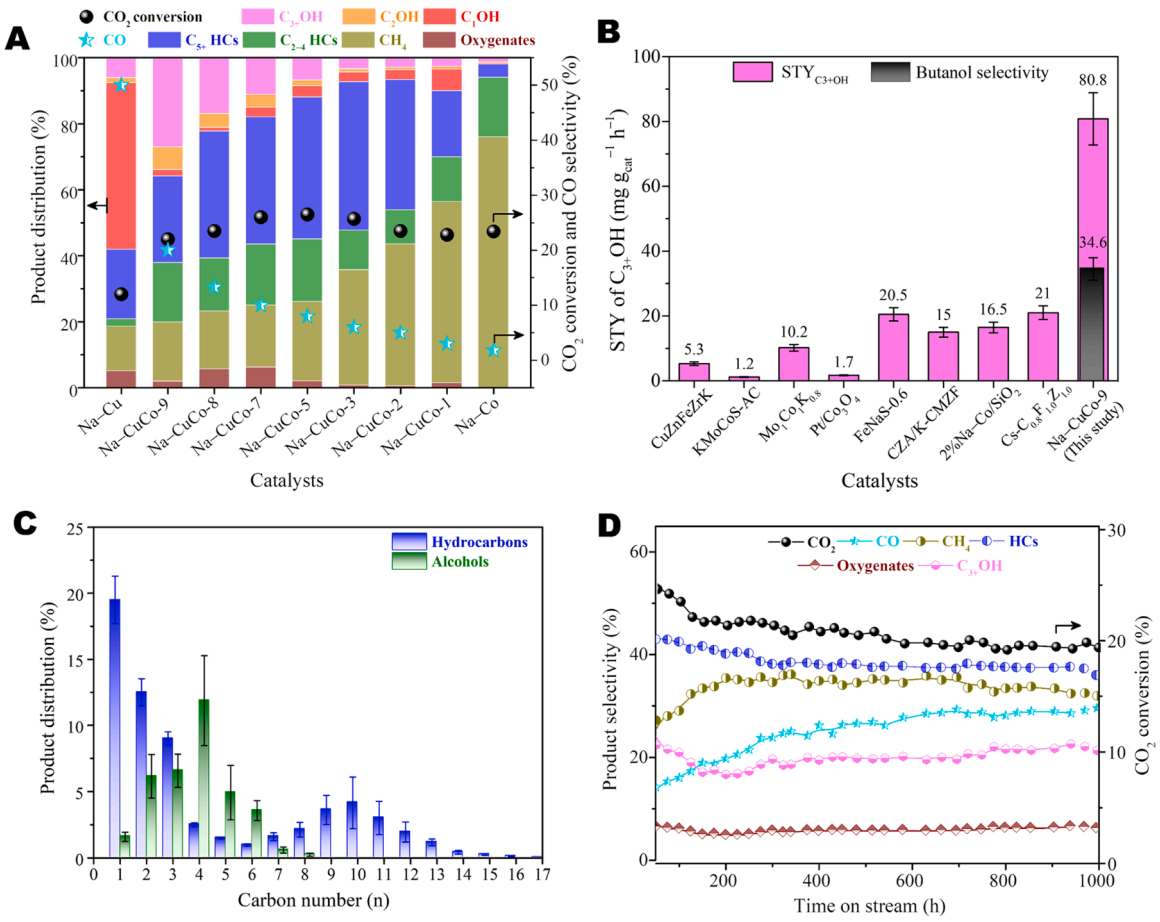

Fig. 1. (A) CO_2 conversion and product selectivity over the Na–CuCo-*y* ($y = Cu/(Cu+Co) \times 10$) catalysts with varying Co contents. The data were collected after a 48 h-on-stream reaction. (B) Comparison of the space-time-yields of C_{3+} alcohols (STY_{C3+OH}) synthesized from the direct conversion of CO_2 presented in this work with those available in the open literature: CuZnFeZrK [73], KMoCoS-AC [74], $Mo_1Co_1K_{0.8}$ [75], Pt/Co_3O_4 [76], FeNaS-0.6 [77], CZA/K-CMZF [78], 2%Na–Co/SiO_2 [79], Cs-$C_{0.8}F_{1.0}Z_{1.0}$ [57], and Na–CuCo-9 (this study). (C) Distribution of alcohols and hydrocarbons produced over the Na–CuCo-9 catalyst with respect to carbon number (*n*). (D) Long-term stability test of the Na–CuCo-9 catalyst during CO_2 hydrogenation. Reduction conditions: Ramp rate of 2.5 °C min^{-1}, 350 °C, 4.0 MPa, H_2 flow rate of 30 mL min^{-1} for 12 h. Reaction conditions: 330 °C, 4.0 MPa, H_2/CO_2 ratio of 1:1, GHSV of 2000 mL g^{-1} h^{-1} (CO_2 = 1000 mL g^{-1} h^{-1}; H_2 = 1000 mL g^{-1} h^{-1}).

toward gaseous C1 products decreased, whereas that toward $C_{3+}OH$ and C_{5+} hydrocarbons increased. This result indicates that a high reaction pressure increases the coverage of the CH_x moieties over the Na–CuCo-9 catalyst, thereby facilitating the C–C coupling reaction by suppressing the desorption of CH_x as CH_4.

To further verify the role of the C/H ratio on $C_{3+}OH$ selectivity, we examined the effect of the H_2/CO_2 ratio under identical GHSV conditions (Fig. S2C). When the H_2/CO_2 ratio was increased from 0.5 to 4, the CO_2 conversion increased from 12.0% to 29.1%, whereas CO selectivity decreased from 35.0% to 10.0%. However, at a high H_2/CO_2 ratio of 4, CH_4 and paraffinic C_{2+} hydrocarbons were the dominant products. Moreover, a negligible fraction of alcoholic species was formed, likely because of the decrease in C/H coverage on the catalyst surface. A high $C_{3+}OH$ yield was obtained when the C/H coverage was controlled by adjusting the H_2/CO_2 ratio to 1.

When the GHSV was increased from 2000 to 12,000 mL g_{cat}^{-1} h^{-1}, CO_2 conversion decreased from 22.1% to 15.0%, CO selectivity increased from 20.8% to 40.0%, and $C_{3+}OH$ selectivity decreased from 27.4% to 3.0% (Fig. S2D). In the context of $C_{3+}OH$ productivity over a given time, the STY_{C3+OH} achieved at a GHSV of 5000 mL g_{cat}^{-1} h^{-1} (80.8 mg g_{cat}^{-1} h^{-1}) was approximately two times larger than that at a GHSV of 2000 mL g_{cat}^{-1} h^{-1} (Table S1); however, further increases in GHSV decreased STY_{C3+OH}. At a high GHSV, the adsorbed CO* produced by RWGS was flushed out of the system instead of participating in the subsequent reaction, with the yields of $C_{3+}OH$ and CO decreasing and increasing, respectively.

3.2. Catalyst characterization

To investigate the structural variations in the Na–CoCu-9 catalyst during CO_2 hydrogenation, we examined the catalyst samples obtained after calcination in air, reduction in H_2, and CO_2 conversion using X-ray diffraction (XRD). The calcined Na–CoCu-9 catalyst exhibited mixed CuO (JCPDS #48–1548) and Co_3O_4 (JCPDS #43–1003) phases, as shown in Fig. 2. After reduction, the peak associated with CuO and Co_3O_4 disappeared, whereas intense peaks appeared at 43.4°, 50.5°, and 74.2°, corresponding to the (111), (200), and (220) planes of metallic Cu^0 (JCPDS #04–0836). Co oxide and metallic Co^0 phases were not observed in the reduced Na–CoCu-9 catalyst, indicating highly dispersed CoO_x ($0 \le x \le 1$) particles on the surface of the Cu^0 domains. The intensity of the Cu^0 peaks was maintained for up to 1000 h of on-stream CO_2 hydrogenation, demonstrating the high resistance of the catalyst to reoxidation. The crystallite size of Cu^0 increased slightly from 24.5 nm in the reduced catalyst to 26.2 nm in the spent catalyst collected after the 1000 h-on-stream reaction (Table S3), indicating that crystal growth was highly suppressed. A closer inspection of the XRD pattern in Fig. 2B revealed the presence of CoO in the spent catalysts, indicating that some metallic Co^0 was oxidized during the CO_2

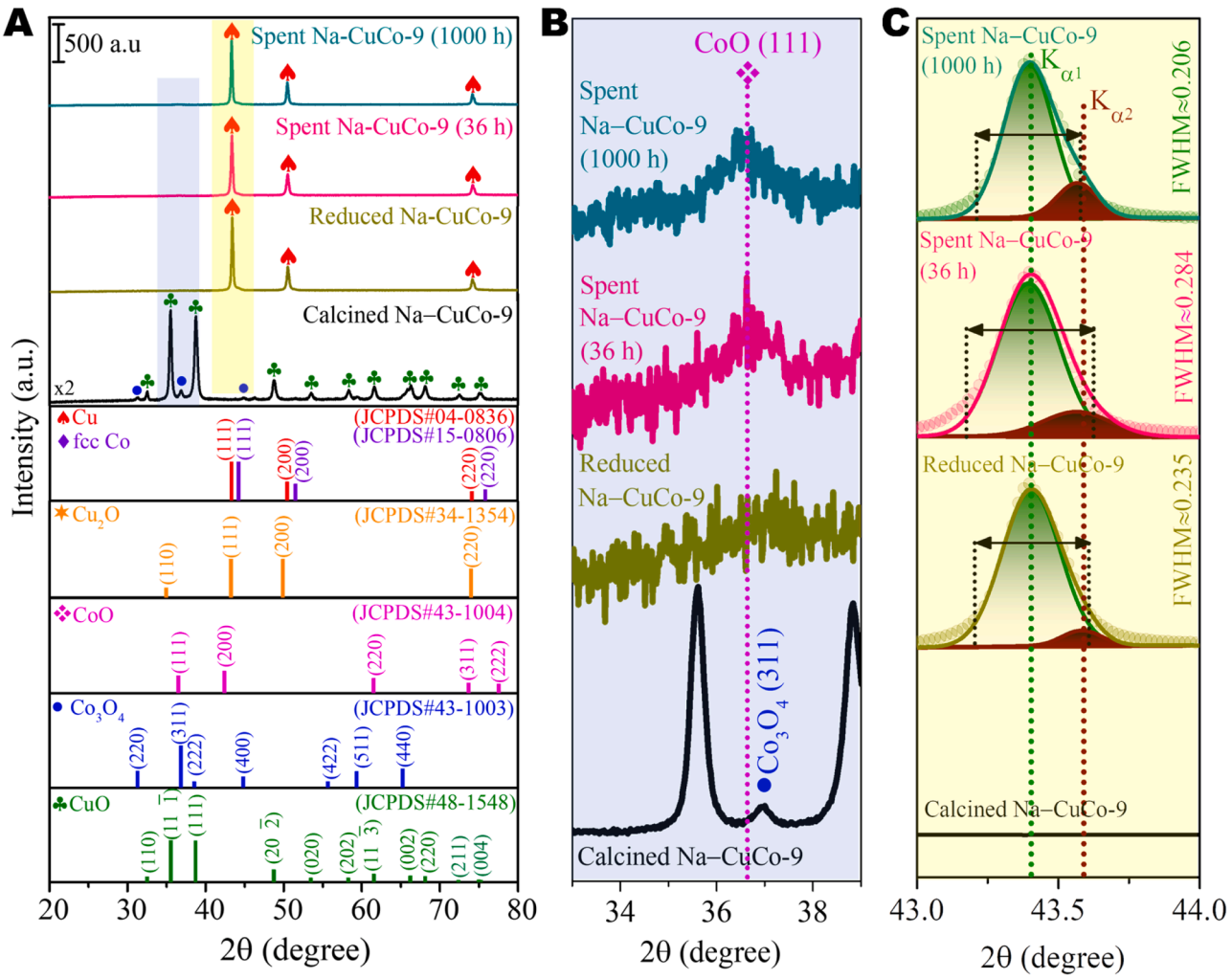

Fig. 2. (A) XRD patterns of the calcined, reduced, and spent Na–CuCo-9 catalysts collected after 36 and 1000 h-on-stream reactions, (B) disappearance of Cu oxide phases in the reduced and spent catalysts, and emergence of the CoO phase in the spent catalysts, and (C) distinct peak-splitting of the Cu(111) Kα-1 and Kα-2 peaks in the spent Na–CuCo-9 catalyst owing to the growth of the metallic Cu^0 phase during CO_2 hydrogenation. (FWHM- Full width at half maximum). Reduction conditions: Ramp rate of 2.5 °C min^{-1}, 350 °C, 4.0 MPa, H_2 flow rate of 30 mL min^{-1} for 12 h. Reaction conditions: 330 °C, 4.0 MPa, H_2/CO_2 ratio of 1:1, GHSV of 2000 mL g^{-1} h^{-1} (CO_2 = 1000 mL g^{-1} h^{-1}; H_2 = 1000 mL g^{-1} h^{-1}).

hydrogenation. In addition, during CO_2 hydrogenation, the progressive splitting of the Cu(111) peak was observed (Fig. 2C) due to grain growth and strain evolution [37].

The XRD patterns of calcined monometallic and bimetallic catalysts with varying Cu/Co ratios are presented in Fig. S3. The calcined Na–Cu catalyst exhibited the characteristic peaks associated with pure CuO. As the Co content in the Na–CuCo-*y* catalysts increased, the intensity of the CuO peaks decreased, whereas the peaks associated with Co_3O_4 increased. The possibility of solid solution (for example, the $Cu_xCo_{3-x}O_4$ species) formation in the calcined Na–CuCo-*y* catalysts was excluded because the peaks associated with CuO and Co_3O_4 were not shifted. When *y* in the calcined Na–CuCo-*y* catalysts was decreased from 9 to 1, the crystallite sizes of Co_3O_4 slightly increased from 18.7 to 26.9 nm, but that of CuO did not change significantly (18.4–20.4 nm, Table S3).

When the Cu content in the reduced Na–CuCo-*y* catalysts was decreased, the crystallite size of Cu^0 decreased from 24.5 (Na–Cu) to 17.2 nm (Na–CuCo-1), indicating that the presence of Co suppressed the crystal growth of Cu^0 (Fig. S4, Table S3). The evolution of the peak associated with face-centered cubic (FCC) Co^0 (JCPDS #15–0806) was observed in the Na–CuCo-*y* catalysts with $y \leq 7$, whereas the presence of hexagonal close-packed (HCP) Co^0 was only observed in the Co-rich Na–CuCo-*y* catalysts with $y \leq 1$. A closer inspection revealed that the FCC Co^0(111) and HCP Co^0(100) peaks downshifted in the bimetallic Na–CuCo-*y* ($1 \leq y \leq 7$) catalysts than those in the Na–Co catalyst (Fig. S4B), indicating the formation of Cu–Co alloys during the reduction reaction. Residual CuO was observed in the reduced Na–Cu catalyst, whereas the peaks associated with $Cu^{\delta+}$ and $Co^{\delta+}$ oxides were not observed in the reduced Na–CuCo-*y* and Na–Co catalysts; this finding illustrates that the presence of Co facilitates the reduction of Cu oxide phases. Following the transformation of $Co^{\delta+}$ oxides into metallic Co^0, dissociative H_2 adsorption on Co^0 nanoparticles and H spillover to the Cu domain activated the reduction of $Cu^{\delta+}$ oxides [38].

In the spent Na–CuCo-*y* ($1 \leq y \leq 7$) catalysts collected after a 36 h-on-stream reaction, the peaks associated with FCC Co^0(111) and HCP Cu^0(111) shifted back to the angle positions observed in their pure state (Fig. S5), signifying that dealloying and phase segregation occurred during CO_2 hydrogenation. As in the case of the spent Na–CuCo-9 catalyst collected after the 1000 h-on-stream reaction, the presence of CoO(111) was observed in the spent Co-rich Na–CuCo-1 and Na–Co catalysts collected after the 36 h-on-stream reaction. As the Co content increased, the clear evolution of FCC Co^0(111) and HCP Co^0(100) was observed in the spent catalysts.

The local chemical structures of Cu and Co in the catalysts were analyzed using X-ray absorption spectroscopy (XAS). The Cu K-edge X-ray absorption near-edge structure (XANES) spectrum of the calcined Na–CuCo-9 catalyst exhibited a weak pre-edge peak at 8977.3 eV and a

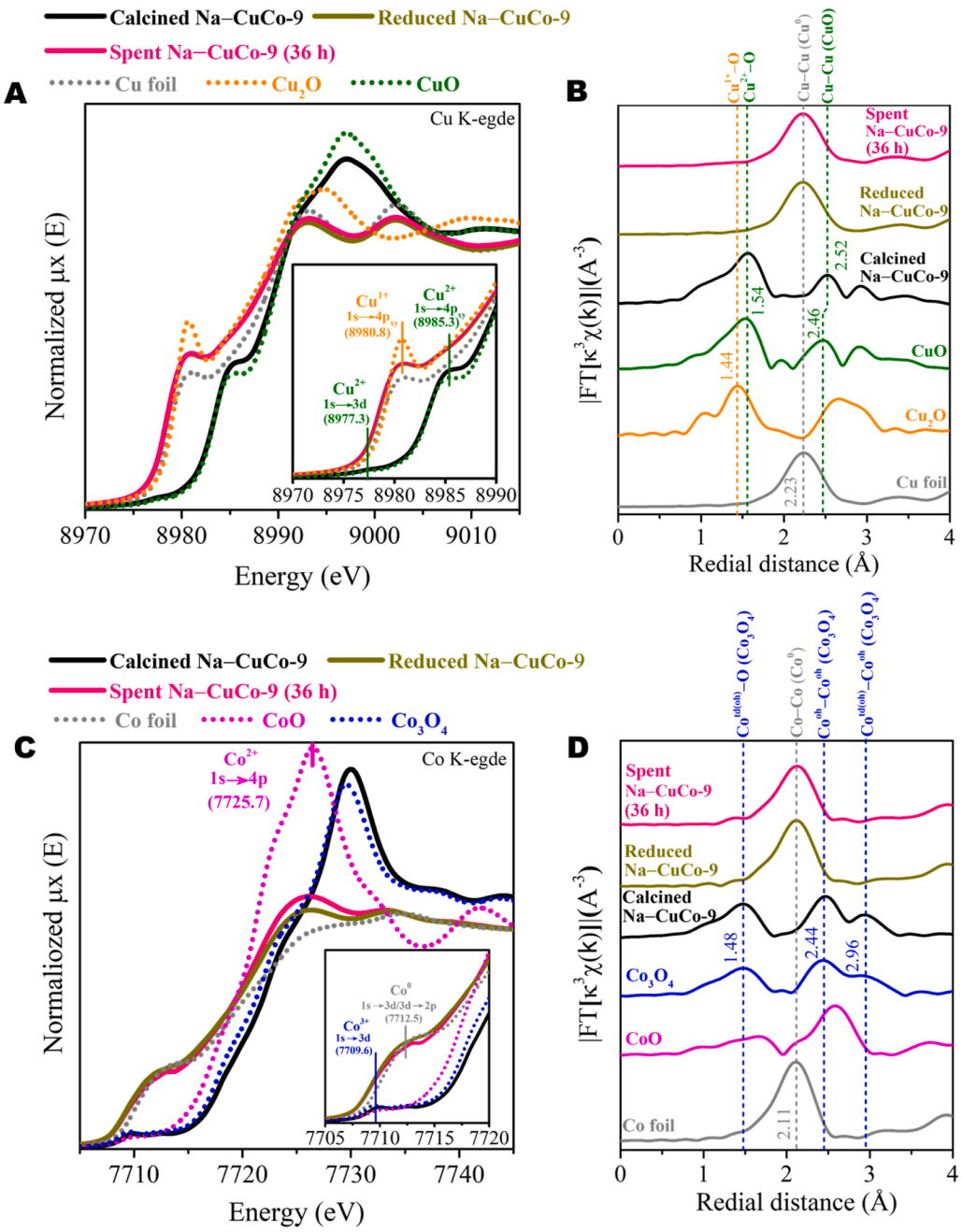

Fig. 3. (A) Normalized Cu K-edge XANES spectra of the calcined, reduced, and spent Na–CuCo-9 catalysts, (B) Fourier transform of the k^3-weighted Cu K-edge EXAFS spectra of the calcined, reduced, and spent Na–CuCo-9 catalysts, (C) normalized Co K-edge XANES spectra of the calcined, reduced, and spent Na–CuCo-9 catalysts, and (D) Fourier transform of the k^3-weighted Co K-edge EXAFS spectra of the calcined, reduced, and spent Na–CuCo-9 catalysts. Reduction conditions: Ramp rate of 2.5 °C min^{-1}, 350 °C, 4.0 MPa, H_2 flow rate of 30 mL min^{-1} for 12 h. Reaction conditions: 330 °C, 4.0 MPa, H_2/CO_2 ratio of 1:1, GHSV of 2000 mL g^{-1} h^{-1} (CO_2 = 1000 mL g^{-1} h^{-1}; H_2 = 1000 mL g^{-1} h^{-1}).

relatively strong absorption peak at 8985.3 eV, which corresponds to the dipole-forbidden 1 s → 3d and dipole-allowed 1 s → $4p_{xy}$ electron transitions of $Cu^{(2+)}O$, respectively (Fig. 3A) [39]. The XANES spectra of the reduced and spent catalysts exhibited features similar to those of Cu foil, indicating that the Na–CuCo-9 catalyst retained the metallic FCC Cu^0 phase well during CO_2 hydrogenation. The k^3-weighted Fourier-transformed (FT) magnitudes of the Cu K-edge extended X-ray absorption fine structure (EXAFS) spectra (Fig. 3B) of the calcined Na–CuCo-9 catalyst and its corresponding references showed an intense peak at 1.54 Å, corresponding to the Cu–O first-shell scattering path of $Cu^{(2+)}O$. The Cu–Cu scattering path of the CuO standard at 2.46 Å was slightly upshifted to 2.52 Å in the calcined Na–CuCo-9 catalyst, which can be attributed to the presence of disordered domains. The reduced and spent Na–CuCo-9 catalysts exhibited an intense peak at 2.23 Å, corresponding to the Cu–Cu scattering path of Cu^0. In particular, the spent catalyst did not exhibit the scattering paths associated with Cu oxides. The Cu^0 content in the spent Na–CuCo-9 catalyst was > 98%, which was calculated via the linear combination fitting of the XANES spectra (Table S4). Thus, during CO_2 hydrogenation, the reoxidation of Cu^0 to $Cu^{\delta+}$ oxide phases was highly suppressed. To examine the presence of Cu oxides, we further analyzed the EXAFS data; the k^3-weighted FT magnitudes of the normalized Cu K-edge EXAFS spectra ($\kappa^3\chi(k)$) of the reduced and spent Na–CuCo-9 catalysts are shown in Fig. S6. The intensity of the Cu–Cu scattering peak was significant, whereas that of the Cu–O shell scattering peak was negligible. The slight decrease in the coordination numbers (CNs) of Cu–Cu in the spent catalyst was attributed to the slight tendency of its surface to reoxidize with the formation of $Cu_2^{(1+)}O$ (Table S5). Thus, metallic Cu^0 is the dominant species in the spent Na–CuCo-9 catalyst, with a fine film of $Cu_2^{(1+)}O$ covering the Cu^0 domains.

The Co K-edge XANES spectrum of the calcined Na–CuCo-9 catalyst exhibited a pre-edge peak at 7709.6 eV, which can be attributed to the

1 s → 3d dipole-forbidden electron transition that is allowed in tetrahedral Co^{2+} sites [40] (Fig. 3C). In the reduced and spent Na–CuCo-9 catalysts, pre-edge peaks were observed at 7712.5 eV, which corresponds to the 1 s → 3d/3d → 4p electron transitions of Co^0 [40]. The intensity of the white line peak at 7725.7 eV, attributed to the 1 s → 4p dipole-allowed electron transition of $Co^{(2+)}O$,[41] slightly increased in the spent catalyst than those in the reduced catalyst and Co foil reference; thus, a small fraction of CoO formed on the metallic Co^0 domains in the spent catalyst. The k^3-weighted FT magnitudes of the Co K-edge EXAFS spectra of the Na–CuCo-9 catalysts show that the transition of Co_3O_4 (calcined) to Co^0 (reduced and spent) occurs in the bulk Co phase during CO_2 hydrogenation (Fig. 3D). The metallic Co^0 content calculated from the linear combination fitting of the XANES spectra was > 97% (Table S4), denoting that the bulk Co phase in the spent Na–CuCo-9 catalyst was mainly metallic in nature. The CN for Co–Co in FCC Co^0, which was determined by fitting the ($\kappa^3\chi$(k)) EXAFS spectra (Fig. S7), slightly increased from 6.8 (reduced) to 6.9 (spent, 36 h, Table S6), thus supporting the deduction that the metallic Co^0 phase was retained during CO_2 hydrogenation.

Changes in the electronic states and chemical environment of the catalyst surface during reduction and CO_2 hydrogenation were monitored using ultra-high vacuum X-ray photoelectron spectroscopy (UHV-XPS). The high-resolution Cu 2p XPS profile of the calcined Na–CuCo-9 catalyst exhibited two main peaks at 933.7 and 953.5 eV, corresponding

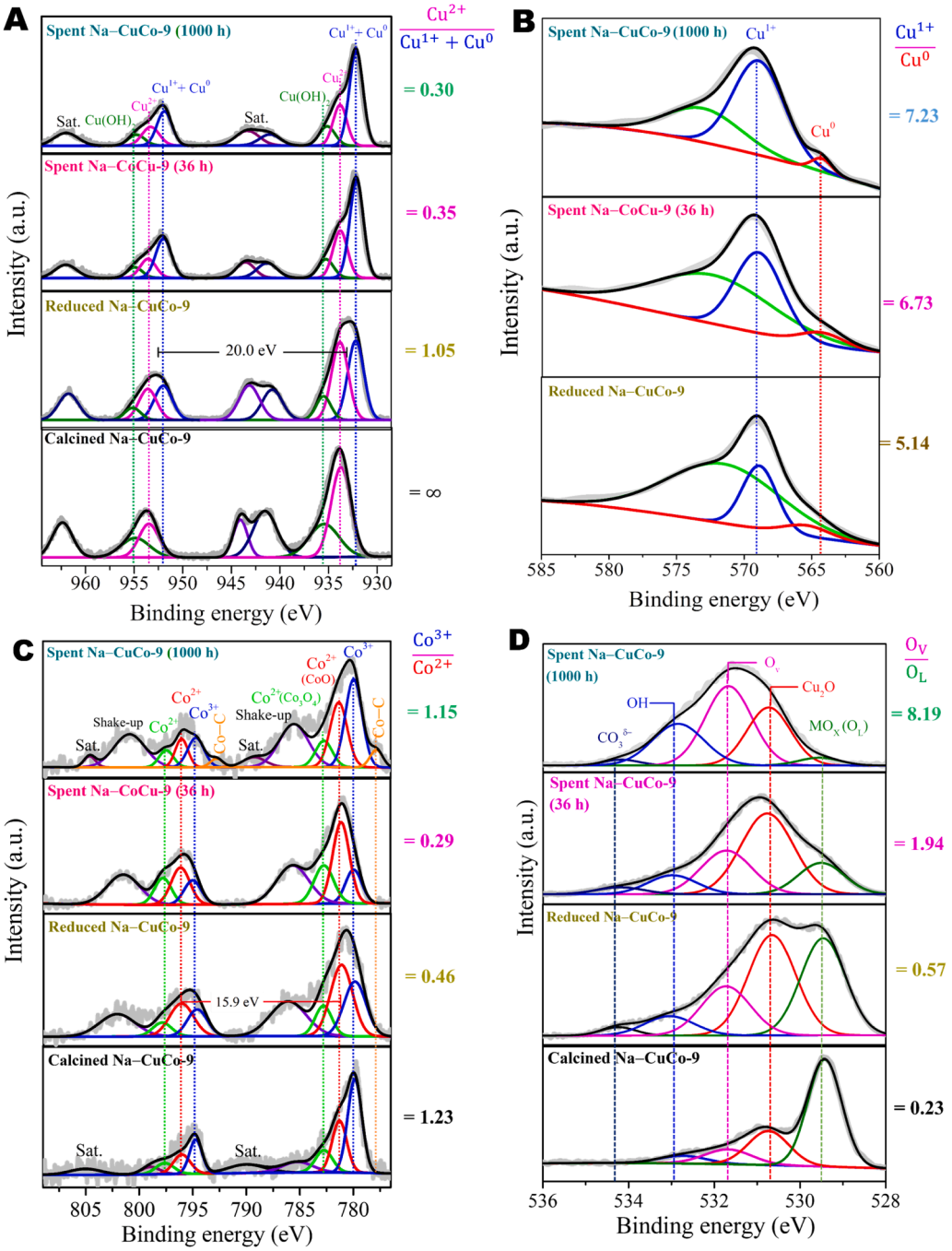

Fig. 4. (A) Cu 2p, (B) Cu LMM, (C) Co, and (D) O 1 s XPS spectra collected from the calcined, reduced, and spent Na–CuCo-9 catalysts. Reduction conditions: Ramp rate of 2.5 °C min^{-1}, 350 °C, 4.0 MPa, H_2 flow rate of 30 mL min^{-1} for 12 h. Reaction conditions: 330 °C, 4.0 MPa, H_2/CO_2 ratio of 1:1, GHSV of 2000 mL g^{-1} h^{-1} (CO_2 = 1000 mL g^{-1} h^{-1}; H_2 = 1000 mL g^{-1} h^{-1}).

to $2p_{3/2}$ and $2p_{1/2}$ of $Cu^{(2+)}O$, respectively (Fig. 4A) [42]. Additional peaks at 935.4 and 954.9 eV can be assigned to Cu $2p_{3/2}$ and Cu $2p_{1/2}$ of $Cu(OH)_2$, respectively. The intense shake-up transition peaks near 943 and 967 eV confirmed the presence of Cu^{2+} species with incompletely filled 3d shells [42]. The reduced Na–CuCo-9 catalyst exhibited peaks at low binding energies of 932.1 and 951.9 eV, which can be attributed to the reduction of Cu^{2+} species to Cu^{1+}/Cu^0. Because of the difficulty in differentiating Cu^{1+} from Cu^0 in the Cu 2p XPS profiles, we collected Auger Cu $2p_{3/2}$ LMM (L-inner level-M-inner level-M-inner level electron transition) spectra for further analysis (Fig. 4B) [42]. Both Cu^{1+} and Cu^0 species were present in the reduced Na–CuCo-9 catalyst. The intensity of the Cu^{2+} and satellite peaks in the spent Na–CuCo-9 catalyst collected after the 36 h-on-stream reaction demonstrated a significant decrease, whereas the intensity of the peaks associated with (Cu^0 + Cu^{1+}) species showed an increase. Thus, the $Cu^{2+}/(Cu^0 + Cu^{1+})$ ratio decreased from 1.05 (reduced) to 0.35 (spent, 36 h). Notably, the $Cu^{2+}/(Cu^0 + Cu^{1+})$ ratio (0.30) did not change significantly after the 1000 h-on-stream reaction. The presence of metallic Cu^0 in the spent catalyst was confirmed by the Auger Cu $2p_{3/2}$ LMM spectra. However, the Auger spectra and difference in binding energy between Cu $2p_{1/2}$ and Cu $2p_{3/2}$ (20.0 eV) indicated that tetrahedral Cu^{1+} was the dominant species on the surface of the reduced and spent catalysts [43].

In the Co $2p_{3/2}$ spectrum of the calcined, reduced, and spent Na–CuCo-9 catalysts (Fig. 4C), the peaks at 779.8/794.7, 780.1/795.3, and 782.6/797.5 eV can be assigned to $2p_{3/2}/2p_{1/2}$ of $Co_3^{(3+)}O_4$, $Co^{(2+)}O$, and $Co_3^{(2+)}O_4$, respectively [44]. Compared with those in the

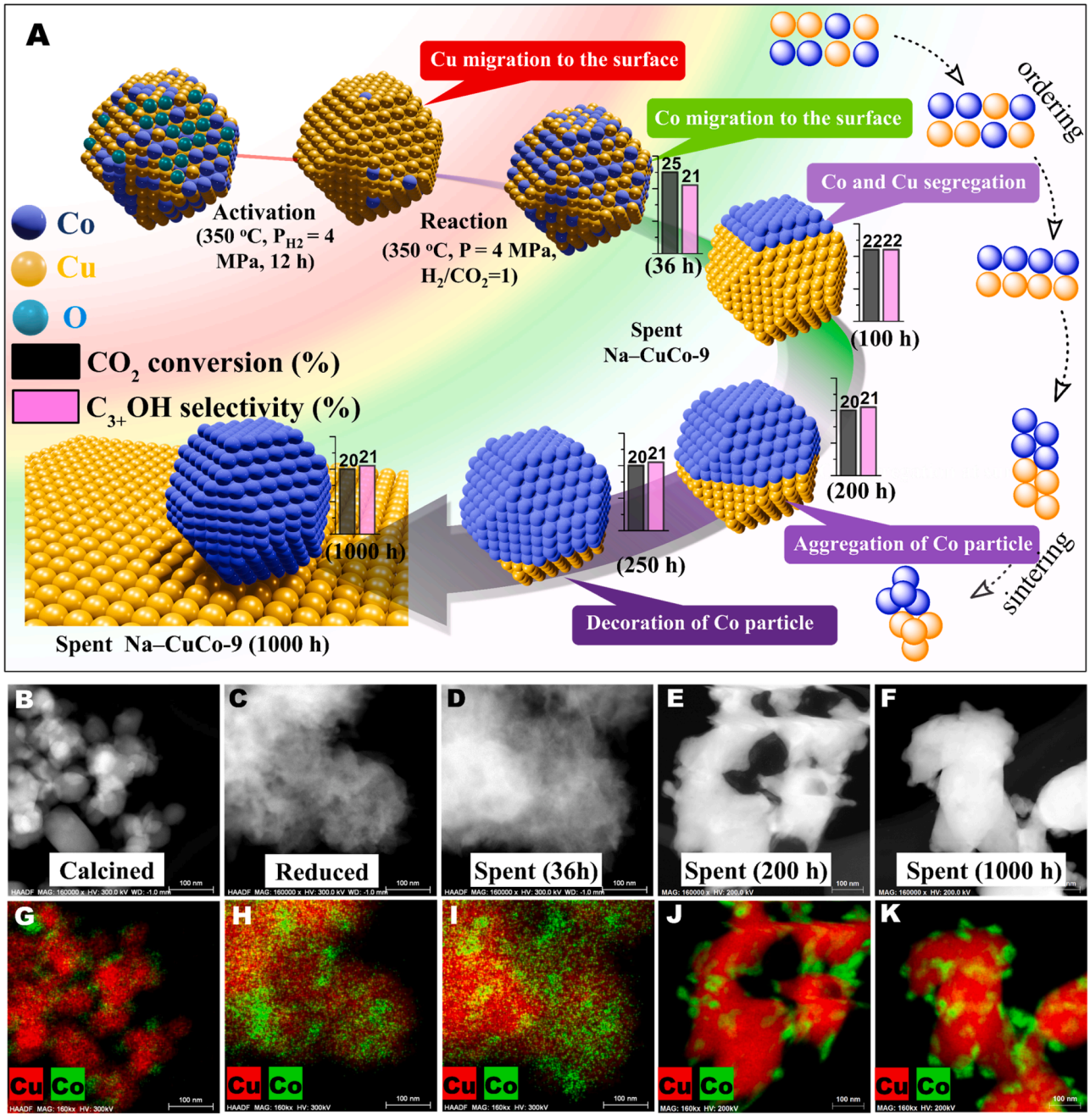

Fig. 5. (A) Schematic of the morphological reconstructing of the catalyst during calcination, reduction, induction, and long-term hydrogenation. (B)–(F) HAADF-STEM images and (G)–(K) their corresponding EDS images of the Na–CuCo-9 catalysts. Reduction conditions: Ramp rate of 2.5 °C min^{-1}, 350 °C, 4.0 MPa, H_2 flow rate of 30 mL min^{-1} for 12 h. Reaction conditions: 330 °C, 4.0 MPa, H_2/CO_2 ratio of 1:1, GHSV of 2000 mL g^{-1} h^{-1} (CO_2 = 1000 mL g^{-1} h^{-1}; H_2 = 1000 mL g^{-1} h^{-1}).

reduced catalyst, the intensity of the $Co_3^{(3+)}O_4$ peak decreased, whereas that of the $Co^{(2+)}O$ peak increased, in the spent catalyst collected after the 36 h-on-stream reaction. The evolution of tetrahedral Co^{2+} species in the spent catalyst can be confirmed by the binding energy gap of 15.9 eV between Co $2p_{3/2}$ and Co $2p_{1/2}$ [45]. Thus, the $Co^{(2+)}O/Co_3^{(3+)}O_4$ ratio decreased from 0.46 (reduced) to 0.29 (spent, 36 h). The evolution of a small peak at 778.4 eV in the spent catalyst collected after the 1000 h-on-stream reaction can be attributed to the formation of the Co–C bond [46], which was evident in the C 1 s spectra of the spent catalysts (Fig. S8A). The survey XPS spectra show that residual Cl was not detected (Figs. S8B and C). The O 1 s spectra of the Na–CuCo-9 catalysts can be deconvoluted into lattice oxygen (O_L), Cu_2O, oxygen vacant sites (O_v), CO, and H_2O_{Phy} at 529.3, 530.4, 531.5, 532.6 and 533.8 eV, respectively (Fig. 4D) [47]. The O_v/O_L ratio increased from 0.57 (reduced) to 1.94 (spent, 36 h) and then to 8.19 (spent, 1000 h). This finding confirms once more that a reducing environment was created during CO_2 hydrogenation. Thus, the XRD, XAS, and XPS analyses collectively revealed that the bulk phases of the calcined Na–CuCo-9 catalysts consisted of CuO and Co_3O_4 without any hint of alloying, whereas the spent catalyst consisted of metallic Cu^0 and Co^0 phases, together with tiny domains of partially oxidized $Cu^{\delta+}$ and $Co^{\delta+}$.

Morphological changes in the calcined, reduced, and spent Na–CuCo-9 catalysts were examined using high-resolution transmission electron microscopy (HR-TEM) and high-angle annular dark-field scanning transmission electron microscopy (HAADF-STEM) coupled with energy-dispersive X-ray spectroscopy (EDX). The overall structural changes of the catalyst are summarized in Fig. 5. In the calcined catalyst, Co_3O_4 particles measuring 10–30 nm in size were deposited on the surface of CuO particles measuring 100–150 nm in size (Fig. S9). The increase in Co contents in the Na–CuCo-*y* catalysts resulted in the growth of Co_3O_4 domains (Figs S10 and S11). During reduction, some CuO and Co_3O_4 were transformed into their corresponding metallic Cu^0 and Co^0 phases containing partially reduced $Cu^{\delta+}$ and $Co^{\delta+}$ oxides at the outermost surface (Fig. S12). The Cu_2O phase grew in a bow-wave manner and generated surface kinks toward the periphery of the Cu particles (Fig. S12C). The atomic Cu/Co ratio at the surface of the reduced catalyst increased to 5.1 compared with that of the calcined catalyst (4.6, Table S7), denoting that the Cu domains migrated to the outermost surface of the material during reduction. By contrast, the atomic Cu/Co ratio in the spent catalyst collected after the 36 h-on-stream reaction decreased significantly to 2.5 (Table S7), indicating that Co domains migrated preferentially toward the outermost surface of the material during CO_2 hydrogenation.

The segregation of FCC Co domains on the surface of $Cu^{\delta+}/Cu^0$ particles was observed in the spent catalyst (Fig. S13). The preferential adsorption of RWGS-produced CO on the Co^0 site could be responsible for the surface enrichment of Co [48]. The growth of Co^0 domains on the surface of $Cu^{\delta+}/Cu^0$ particles (observed as CO_2 hydrogenation) continued for 200 h (Fig. S14). The spent catalyst collected after the long-term reaction of 1000 h showed no significant change in the size of Cu and Co domains compared with that observed after 200 h (Fig. S15); after the 1000 h on-stream reaction, $Co^{\delta+}/Co^0$ particles measuring 20–30 nm in size were uniformly decorated on the Cu surface. Thus, after its morphological reconstruction in the initial period of the reaction, the catalyst maintained its morphology over the subsequent long-term CO_2 hydrogenation. Segregation of Cu and Co domains, migration of Co toward the periphery, and aggregation at the outermost surface continued during CO_2 hydrogenation (Fig. 5A). The restructuring of the catalyst continued until the Co particles were decorated on the stabilized Cu domains, and the size of the Co particles eventually increased from 6 nm (36 h) to 15–20 nm (200 h). The Co particles maintained their size for up to 1000 h. Thus, the initial 200 h of CO_2 hydrogenation can be considered an "induction" period in which the catalyst was reconstructed. Thus, the initial decrease in the CO_2 conversion can be attributed to the decrease in the active catalytic surface area due to sintering. A close inspection of the Cu phase in the spent catalyst (1000 h) revealed the existence of both Cu^0 and Cu_2O phases (Figs. S15D and H, respectively).

3.3. Reaction intermediates and mechanisms

3.3.1. Surface oxidation states and reaction intermediates

Based on the ex situ analyses, the surface of the catalyst during CO_2 hydrogenation consisted of Cu^0/Cu^{1+} and Co^0/Co^{2+}. Nonetheless, the change in oxidation states of the spent catalyst upon exposure to air impedes our understanding of the actual nature and metallic-to-oxide proportions of the catalyst surface. Thus, to examine the real-time oxidation states of Cu and Co on the catalyst surface as well as the reaction intermediates formed during CO_2 hydrogenation, we performed near-ambient pressure XPS (NAP-XPS). The Na–CuCo-9 catalyst was pre-reduced in the fixed-bed reactor prior to its transfer to the NAP-XPS chamber. Carbonaceous impurities on the catalyst surface were removed in the chamber by in situ oxidation, after which the catalyst was reduced in situ (Fig. S16). Thus, the evolution of C-containing species during CO_2 hydrogenation could be attributed exclusively to the reaction intermediates and products. After in situ oxidation, the temperature-dependent reduction behavior of the Na–CuCo-9 catalyst showed a significant decrease in the intensity of O_L at 529.2 eV, but a small fraction of O_L persisted in the material (Fig. S17); this finding indicates the incomplete reduction of Cu and Co oxides to their corresponding metallic phases. When the reduction time was extended to 90 min at 350 °C, the marked emergence of the $Cu_2^{(1+)}O$ peak at 530.2 eV was observed in the in situ O 1 s XPS profile of the catalyst. The partial reduction of the oxides can be further verified from the temperature-programmed reduction (TPR) results of the calcined Na–CuCo-9 catalyst under a H_2 flow at 350 °C (Fig. S18).

The major Cu species in the in situ reduced Na–CuCo-9 catalyst was $Cu_2^{(1+)}O$, as confirmed by the presence of a Cu $2p_{3/2}$ peak at 932.36 eV (Fig. 6A). During CO_2 hydrogenation, the Cu $2p_{3/2}$ peak was slightly upshifted to 932.61 eV, resulting in a binding energy difference of 19.8 eV between Cu $2p_{1/2}$ and Cu $2p_{3/2}$; this finding validates the presence of Cu^0 in the catalyst during CO_2 hydrogenation [42,43]. The gaseous CO (g-CO) generated by the RWGS reaction in situ facilitated the reduction of Cu_2O (Cu^{1+}) to Cu^0 [49], as confirmed by the CO-TPR results (Fig. S19). The very weak intensity of the satellite peaks further confirmed that the surface of the Na–CuCo-9 catalyst consisted mainly of Cu^0/Cu^{1+}. Thus, the presence of $Cu^{(2+)}O$ and $Cu_2^{(1+)}O$, which were detected as the major surface species in the UHV-XPS profiles of the spent catalyst (Fig. 4B), could be attributed to surface passivation when the spent catalyst was exposed to ambient air. The emergence of Cu^0 during CO_2 hydrogenation suggests that a redox cycle occurred on the catalyst surface [50].

As shown in Fig. 6B, $Co_3^{(3+)}O_4$ and $Co^{(2+)}O$ species coexisted in the in situ reduced catalyst. The intensity of the peak associated with $Co^{(2+)}O$ and $Co_3^{(3+)}O_4$ during CO_2 hydrogenation increased and decreased significantly, respectively, which can be attributed to the enhanced reduction caused by CO (Fig. S19). Moreover, the emergence of the peak at 778.2 eV during CO_2 hydrogenation can be attributed to the formation of a Co–C bond.

The evolution of reaction intermediates was examined in the O 1 s and C 1 s profiles (Fig. 6C and D, respectively, Table S8). The peaks of O_L and Cu_2O were maintained at 529.2 and 530.2 eV, respectively, during CO_2 hydrogenation. The intensity of the peak at 531.5 eV increased as the reaction temperature increased to 350 °C, which may be caused by the overlap between O_v and formate species. Likewise, the overlap of the binding energies for carbonate (CO_3^{2-}) species with that of physically adsorbed H_2O (H_2O_{Phy}) at 533.2 eV increased in intensity as CO_2 hydrogenation proceeded. In the C 1 s profile, the broad peak centered at 285 eV can be deconvoluted into three sub-peaks of CH_x at 273.8 eV, C–C at 284.8 eV, and CH_3O^* at 285.6 eV [47,51], thus implying that the RWGS reaction produces CO on the Cu site, and that CO is subsequently

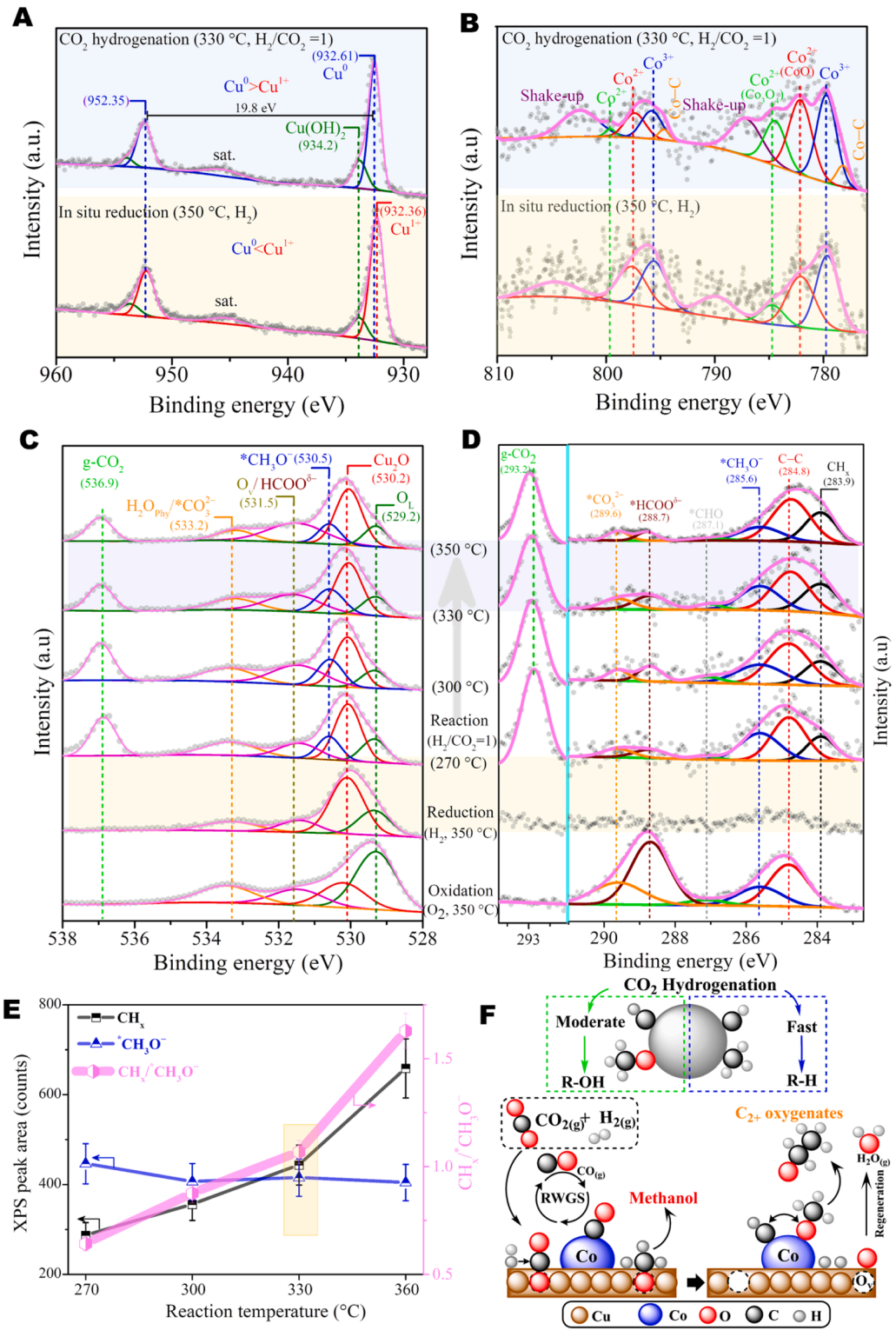

Fig. 6. NAP-XPS profiles of the (A) Cu 2p, (B) Co 2p, (C) O 1 s, and (D) C 1 s regions. (E) CH_x/CH_3O ratio and trends of temperature-dependent surface species obtained from the C 1 s profiles. (F) Schematics of intermediate adsorption and CO_2 hydrogenation. Oxidation conditions: O_2, 350 °C, 100 Pa. Reduction conditions: H_2, 350 °C, 100 Pa. Reaction conditions: CO_2/H_2 ratio of 1:1, 330 °C, 100 Pa.

hydrogenated to CHO* → CH_2O* → CH_3O* [52,53]. The formation of CH_x species can be attributed to the intrinsic property of C–O scission associated with Co^0 [54]. In the carbonate region, the two peaks at 288.7 and 289.6 eV can be assigned to HCOO* and CO_3^{2-}, respectively [55]. The intense peak at 293.2 eV originated from the photoionization of gaseous CO_2 [51].

To understand the temperature dependence of $C_{3+}OH$ selectivity (Fig. S2), we conducted in situ CO_2 hydrogenation at varying temperatures (270–360 °C); the transient responses of intermediates in the C 1 s profiles are summarized in Fig. 6E. The ratio of CH_x to CH_3O* (CH_x/CH_3O*) is strongly temperature dependent and, in turn, controls the selectivity of the reaction toward $C_{3+}OH$. As the temperature increased

from 270° to 330°C, the CH_x/CH_3O^* ratio increased monotonically from 0.64 to 1.05, indicating preferential hydrogenation to form CH_x species at the high-temperature region. Considering that the co-adsorption of dissociated and nondissociated CO is a prerequisite for higher alcohol synthesis [20,56], the near-equimolar CH_x/CH_3O^* balance of ~1.05 is responsible for the high-yield production of $C_{3+}OH$. To further verify the C–O dissociation activity of the Na–CuCo-9 catalyst, we conducted the temperature-programmed surface reaction (TPSR) of pre-adsorbed CO over the reduced Na–CuCo-9 under a 5% H_2/Ar flow (Fig. S20). The evolution of CH_4 represents dissociative CO activation, whereas the CO desorption peak indicates nondissociative CO adsorption [57]. The highest signals in both the CO and CH_4 profiles were observed at 300–350 °C, thus revealing that both nondissociated and dissociated CO adsorptions are activated on the catalyst surface near the optimum reaction temperature (330 °C).

The abundance of CH_3O^* species (Fig. 6D), which is a prominent intermediate in the hydrogenation of CO_2 to methanol over typical Cu-based catalysts [17,58,59], at 285.6 eV and 330 °C, is in line with the higher selectivity of the products obtained at ambient pressure toward methanol (Fig. S2B). Thus, the low selectivity for methanol at elevated pressures (Fig. S2B) suggests that CH_3O^* undergoes further chain extension to produce C_{2+} oxygenates (Fig. 6F) [20]. At the optimum temperature of 330 °C, coupling between CH_x and CH_3O^* species led to the formation of C_{2+} species. When the reaction temperature was further increased to 350 °C, increased CH_x formation negatively affected the CH_x/CH_3O^* balance, increasing it to 1.61 (Fig. 6E). Activated hydrogenation at this higher temperature boosted the cleavage of C–O bonds and subsequent formation of CH_x moieties, eventually facilitating the formation of CH_4 and paraffin-rich hydrocarbons, rather than $C_{3+}OH$, even under hydrogen-deficient conditions (Fig. S2A). Thus, based on the highly temperature-sensitive CH_x/CH_3O^* ratios observed in this work, 330 °C is the optimal temperature for high-yield $C_{3+}OH$ production.

To further elucidate the major reaction intermediates and reaction pathways for the formation of $C_{3+}OH$ via CO_2 hydrogenation, we conducted operando diffuse reflectance infrared (IR) Fourier transform (DRIFT) spectroscopy analyses. The surface leaving species were

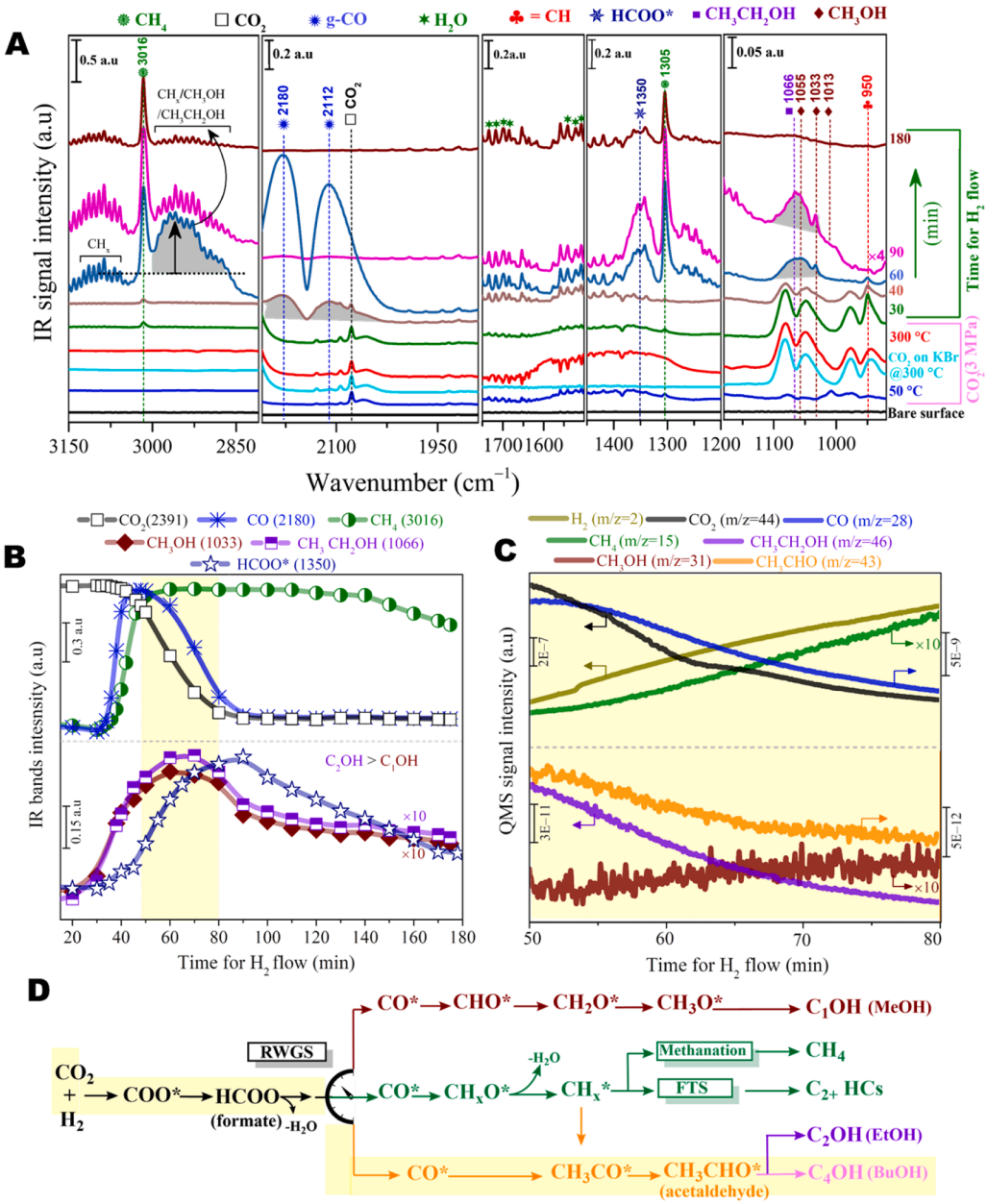

Fig. 7. (A) DRIFT spectra collected during the pressurization of the DRIFT cell with CO_2 at up to 3.0 MPa (blue) at 50 °C. The temperature was then increased up to 300 °C at 3.0 MPa (red), after which the CO_2 gas was switched to H_2 (green and onward) at 300 °C and 3.0 MPa. CO_2 adsorption on KBr at 300 °C (cyan). (B) Adsorbate species that evolved from the pre-adsorbed CO_2 species formed by the H_2 flow over time. (C) QMS-detected species emitted from the DRIFT cell under a H_2 flow of 50–80 min (D) Reaction pathways based on the DRIFT spectra. Pretreatment conditions: Ramp rate of 5 °C min^{-1}, 300 °C, 3.0 MPa, H_2 flow rate of 50 mL min^{-1} for 8 h for reduction, followed by purging with N_2 for 2 h. The DRIFT cell was subsequently cooled to 50 °C. CO_2 adsorption conditions: CO_2 was introduced until the pressure reached 3.0 MPa at 50 °C. The temperature was then increased from 50° to 300 °C at a ramp rate of 5 °C min^{-1}. Hydrogenation conditions: CO_2 was switched to H_2 flowing at a rate of 30 mL min^{-1}.

monitored by a quadrupole mass spectrometer (QMS) installed downstream of the DRIFT cell. Prior to the acquisition of the DRIFT spectra during the CO_2 hydrogenation reaction, the IR spectra of the in situ reduced catalyst were obtained during CO_2 pressurization from 0.1 to 3.0 MPa at 50 °C, followed by an increase in temperature from 50° to 300°C at 3.0 MPa (Figs. S21A and B, respectively) for peak evolution observation and peak identification. The strong peaks at 2400–2200 cm^{-1} and the weak peaks at 2130–2056 cm^{-1} observed during CO_2 pressurization can be attributed to gaseous CO_2 and isotopic CO_2 variants, respectively [60]. The weak peaks at 1082–945 cm^{-1} can also be attributed to gaseous CO_2. The broad bands that emerged at 1409 and 1266 cm^{-1} during CO_2 pressurization can be attributed to the combination bands and overtones of pressurized CO_2 [60], which were significantly blue- and red-shifted, respectively, owing to strong Fermi resonance interactions at the high-pressure region. The intensity of the combination bands decreased with increasing temperature. The band at 1644 cm^{-1}, which appeared when CO_2 was pressurized and could be attributed to H_2O [61], vanished progressively at elevated temperatures.

Following CO_2 adsorption (3 MPa, 300 °C), the gas flow was switched to H_2, and the evolution of reaction intermediates and products was monitored (Fig. 7). The IR bands were assigned on the basis of the adsorption of the probe molecule on the catalyst surface (Fig. S22), and the mass spectra of the effluents were assigned on the basis of their corresponding mass fragments that did not overlap with those of other species (Fig. S23). The evolution of gaseous CO at 2180 and 2112 cm^{-1} [62] was observed after 30 min of H_2 flow (Fig. 7A). Continuous H_2 flow decreased the intensity of the CO band (Fig. 7B) and the CO_2 and CO concentrations in the effluent gases (Fig. 7C). After 30 min of H_2 flow, CH_4 bands appeared at 1305 and 3016 cm^{-1} [63], and the mass signals of CH_4 and H_2 in the effluent gases steadily increased. The bands at 1033 and 1066 cm^{-1}, which were not overlapped with those of CO_2, can be attributed to methanol and ethanol, respectively. The band at 1350 cm^{-1} can be assigned to formate species (HCOO*) [64]. The evolution of CO with the absence of HCOO* after 40 min of H_2 flow implies that formate is not an intermediate for CO formation. The bands associated with COOH* (at ~1620 cm^{-1}) and CH_3O* (at ~1150 cm^{-1}) were not observed in the DRIFT spectra despite the presence of methanol and ethanol in the effluent gas stream; this finding indicates that the adsorbed intermediate species were rapidly converted to the products over the Na–CuCo-9 catalyst. The concentration of ethanol in the effluents was higher than that of methanol, indicating preferential C–C coupling by the CO-inserted CH_x * , which was probably formed by the C–O bond dissociation of CH_xO* intermediates [48]. In addition, the significant amount of acetaldehyde detected in the effluent stream confirmed the high C–C coupling activity, producing acetate intermediates [65]. The formation of CO, methanol, and ethanol was activated by increasing the Co content (Fig. S24) and reaction temperatures (Fig. S25), thereby demonstrating the dependence of product selectivity on the catalyst composition and reaction conditions (Fig. S2).

The Cu surface of the Na–CuCo-9 catalyst is responsible for RWGS, followed by methanol synthesis (Fig. 7D) [66]. Conversely, the Co surface is responsible for the C–O dissociation of CH_xO* to generate CH_x moieties [54], followed by C–C coupling to form CH_3CO* [48]. In addition, the sequential hydrogenation of CH_3CO* can generate acetaldehyde and, eventually, ethanol [48,67,68]. The more favorable formation of C–H than O–H bonds, that is, the easier development of the CHO* versus COH* intermediate during CO* hydrogenation, may be the reason behind the outstanding production of acetaldehyde from CH_3CO* [48,67]. Acetaldehyde serves as a precursor for the formation of ethanol (minor product) or *n*-butanol (major product), which will be discussed in a later section.

3.4. Investigation of intermediates for butanol synthesis

The oxygenated species in the effluent stream were identified as methanol, ethanol, and acetaldehyde. To authenticate potential intermediates for the synthesis of $C_{3+}OH$, we performed controlled reactions using methanol, ethanol, and acetaldehyde as reactants under reaction conditions similar to those used for CO_2 hydrogenation. When the temperature of the DRIFT cell containing pre-reduced Na–CuCo-9 catalyst was raised to 330 °C under a H_2 flow, the pre-adsorbed methanol decomposed into *CH_3 species by protonation, whereas ethanol remained highly stable (Fig. S26). Pre-adsorbed acetaldehyde demonstrated more active decomposition than methanol or ethanol, thereby implying that acetaldehyde may be an active intermediate for the formation of $C_{3+}OH$.

To further investigate the plausible mechanism behind the formation of $C_{3+}OH$, we reacted the probe molecules in a fixed-bed reactor. In the reaction of methanol with H_2, the product stream mainly contained gaseous CO_2, CO, and CH_4. Acetaldehyde and *n*-butanal were detected in the liquid stream, but their peak intensities were very low (Fig. S27A). When ethanol was used as the feed, the main product was 1,1-dimethoxyethane, and *n*-butanal was not observed (Fig. S27B). By contrast, when acetaldehyde conversion was tested, *n*-butanal was the major product (Fig. S27C); this finding indicates that acetaldehyde is the most promising intermediate for *n*-butanol production from CO_2 hydrogenation over the Na–CuCo-9 catalyst.

3.5. Density functional theory analysis

To understand the mechanism underlying the formation of *n*-butanol over the Na–CuCo-9 catalyst, we conducted density functional theory (DFT) simulations of the Co-decorated Cu surface. The CoCu alloying effect on ethanol formation by CO_2 hydrogenation was previously investigated using DFT calculations [69], which showed that the formation of C_2 oxygenates was facilitated at the Co-incorporated step-edge site of Cu(211). Based on these previous findings, the energetics of *n*-butanal formation over the Cu(211) surface with varying amounts of Co decoration were explored in the present study. As shown in Fig. S28, the model surface constructed in this study consisted of Cu(211) and one or more Co atoms substituted with step-edge Cu atoms, which were denoted as Cu(211)-*n*Co ($n = 0, 1, 3, 5$).

Since acetaldehyde is considered the most abundant reaction intermediate in the synthesis of higher alcohols from CO_2 hydrogenation [48,69,70], and was detected in the present study as well, the formation mechanism of *n*-butanol from acetaldehyde as a starting species was investigated. A well-known mechanism is that two acetaldehydes undergo aldol condensation to form crotonaldehyde, which is further reduced to produce *n*-butanal [48,70]. Recently, Ting et al. found that two acetaldehydes could produce *n*-butanal through the crotonaldehyde route with the aid of proton-electron transfer from the electrochemical reduction of CO_2 on Cu/CuO [70]. Another plausible pathway to form C_4 species from two acetaldehydes involves a sequential reaction involving deoxygenation and bond formation. The difference between these two pathways is whether C–C coupling occurs prior to or after the deoxygenation of a C_2 precursor. Herein, the energies of the two pathways were compared to identify the most plausible pathway on the Co-decorated Cu surface. Fig. 8A shows the free-energy diagram for the formation of *n*-butanal through acetaldehyde on the Cu(211)− 1Co surface. All energies and atomistic configurations are shown in Tables S9 and S10 and Figs. S29–S32. Initially, two acetaldehyde molecules undergo a disproportionation reaction to form CH_3CHOH* and CH_2CHO* ((2) → (3)). The kinetic barrier free energy for the (2) → (3) elementary step is 1.03 eV, which is surmountable at the reaction temperature maintained in this study (330 °C). The C–C bond formation between CH_3CHOH* and CH_2CHO* produces CH_3CH* (OH)CH_2CH ((3) → (4)'), which is a precursor state for crotonaldehyde. However, the high kinetic barrier of 1.84 eV for the (3) → (4)' step renders direct C–C bond formation on the Cu(211)− 1Co surface difficult. Hence, the crotonaldehyde pathway (Pathway 1, Fig. 8A) is highly unlikely to be a plausible route for *n*-butanol synthesis from acetaldehyde. As an alternative route, the CH_3CHOH* formed can be chemically dissociated into CH_3CH* and

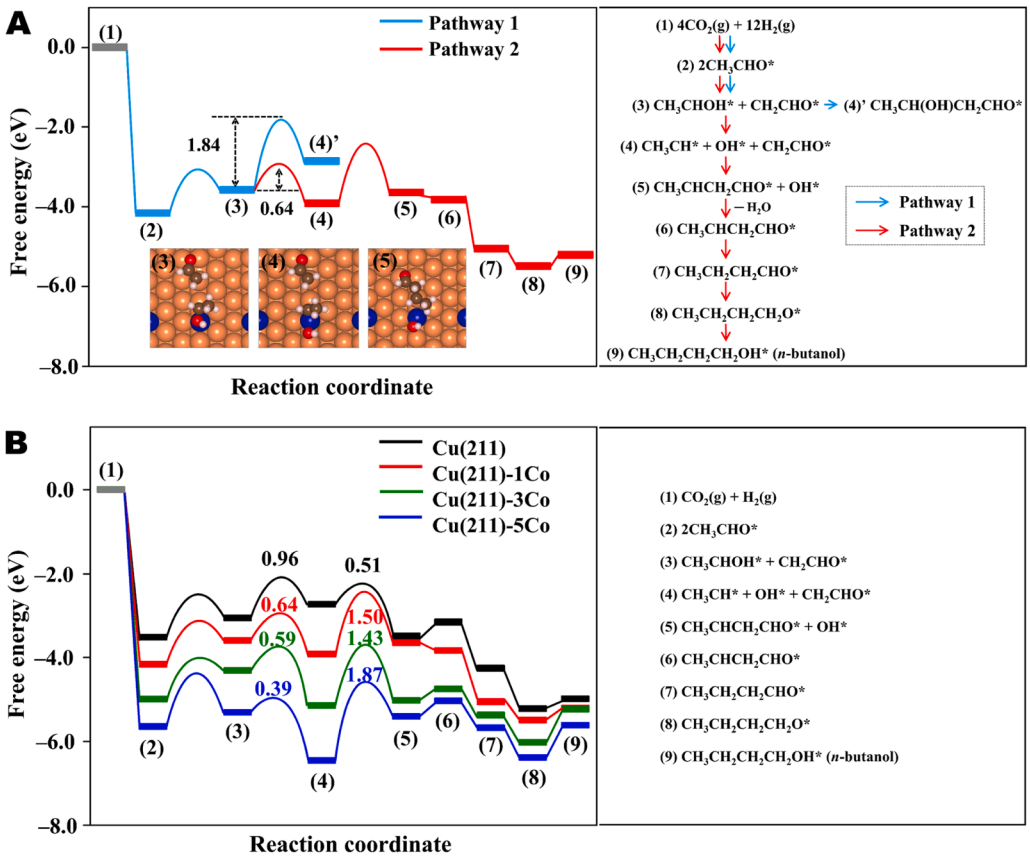

Fig. 8. (A) Free-energy diagram for CO_2 hydrogenation to *n*-butanol through the acetaldehyde reaction on the Cu(211)− 1Co slab. Numbers enclosed in parentheses represent the reaction intermediates. The values in (A) indicate the kinetic barrier free energies for steps (3) → (4) and (3) → (4)'. The insets in (A) depict the top views of (3), (4), and (5). Orange spheres = Cu, blue spheres = Co, brown spheres = C, red spheres = O, light pink spheres = H. (B) Free-energy diagram for CO_2 hydrogenation to *n*-butanol on the Cu(211) surface with different Co contents. The values in (B) indicate the kinetic barrier free energies for steps (3) → (4) and (4) → (5).

OH* ((3) → (4)); in this step, the kinetic barrier energy for CH_3CHOH* dissociation (0.64 eV) is much lower than that for CH_3CH*(OH)CH_2CHO formation. Thus, the C–O bond dissociation of CH_3CHOH, which is denotated as Pathway 2 in Fig. 8A, is energetically more favorable than the crotonaldehyde pathway.

A Co atom located at the step edge site of Cu(211) is responsible for the C–O bond scission of CH_3CHOH*. The CH_3CHOH* intermediate is stabilized at an interfacial Co–Cu site, which is subsequently dissociated on top of a Co atom (insets in (3) and (4) in Fig. 8A). After the dissociation of CH_3CHOH*, the CH_3CH* produced reacts with CH_2CHO* at the Cu site to form CH_3CHCH_2CHO* (inset in (5) in Fig. 8A). The CH_3CHCH_2CHO* intermediate is subsequently hydrogenated to produce *n*-butanol (from step (5) to step (9), Fig. 8A), thus suggesting that a series of bond-breaking and bond-forming reactions occur to produce *n*-butanol on sites where Co and Cu are elaborately combined; that is, C–O bond scission at the Co site to yield unsaturated hydrocarbon species is followed by C–C bond formation between CH_3CH* and CH_2CHO* at the Cu site.

To further understand the effect of the Co configuration on *n*-butanol formation, we investigated the reaction energetics and sequential reactions in Pathway 2 in Fig. 8 over Cu(211) surfaces, with different Co compositions at the step-edge site. Pathway 2 was energetically more favorable than Pathway 1 over all surfaces examined (Fig. S29–S33). Fig. 8B compares the free-energy diagrams for *n*-butanol formation on the Cu(211), Cu(211)− 1Co, Cu(211)− 3Co, and Cu(211)− 5Co surfaces through Pathway 2. The kinetic barriers for the C–O bond dissociation of CH_3CHOH* ((3) → (4)) decreased, whereas the kinetic barrier for C–C bond formation ((4) → (5)) increased, as the Co content increased. For example, acetaldehyde occurred more strongly on the surface of Cu(211)− 5Co, where all step-edge elements were replaced by Co, than on the surface of other slabs; thus, C–O bond cleavage is highly active, whereas C–C bond formation is challenging, on this surface. Therefore, Co-rich surface termination (Cu(211)− 5Co) is unsuitable for *n*-butanol formation. By contrast, on the Cu(211) surface without Co, which only weakly adsorbs reaction intermediates, C–O bond scission is unlikely to occur whereas C–C bond formation occurs relatively easily. Hence, while the Cu(211) surface can be beneficial to *n*-butanol formation, generating C_2 oxygenates (such as acetaldehyde) on this surface through the initial stage of CO_2 hydrogenation is difficult. Therefore, Cu surfaces with moderate Co decorations, such as Cu(211)− 1Co or Cu (211)− 3Co, may be optimal for *n*-butanol formation; the kinetics for *n*-butanol formation can be controlled by the Co–Cu atomistic configuration, which, in turn, determines the critical bond scission and formation kinetics. Our finding of an optimal Co–Cu composition for *n*-butanol formation via DFT simulation agrees well with our experimental observations (Fig. 1A).

To further examine the possibility of *n*-butanol formation by the well-known hydroformylation of propylene (which is the commercial petroleum-based route),[12] we performed DFT simulations of CO* insertion into surface-adsorbed CH_3CHCH_2 * over the Cu(211)− 3Co slab (Fig. S34). Prior to CO insertion, the necessary CO* flipping required an insurmountable kinetic barrier energy (3.51 eV), rendering the hydroformylation route impossible over the Cu(211)− 3Co slab. The possibility of ethanol formation from surface C_2 intermediates was then examined over the Cu(211)− 3Co slab. Fig. S35 shows that the potential reaction pathway for ethanol production was CH_3CHO* → CH_3CH_2O* → CH_3CH_2OH*. However, this pathway is energetically less favorable than the *n*-butanol formation route (Pathway 2, Fig. 8). As shown in Fig. S36, the kinetic barrier for the first hydrogenation step of acetaldehyde (CH_3CHO* → CH_3CH_2O*, $\Delta G_a = 1.27$ eV) was higher than that for its disproportionation to form CH_3CHOH* ($2CH_3CHO$* → CH_3CHOH* + CH_2CHO*, $\Delta G_a = 0.99$ eV). This indicates that the acetaldehyde reaction over the Cu(211)− 3Co slab favors the C_4 pathway rather than the C_2 pathway to form ethanol. Although CH_3CHOH* may be reduced to ethanol, the corresponding kinetic barrier (ΔG_a = 1.17 eV) is much higher than that for the chemical dissociation of

CH_3CHOH^* (ΔG_a = 0.59 eV). Therefore, the facile decomposition of CH_3CHOH^* on the Co–Cu surface accounts for the higher-yield production of *n*-butanol over the Na–CoCu-9 catalyst.

3.6. Catalyst stability for practical applications

The Na–CuCo-9 catalyst exhibited long-term stability, rendering it promising in industrially relevant applications. Surface composition analysis of the spent catalyst revealed that the Na–CuCo-9 catalyst exhibited high resistance against reoxidation. Thermogravimetric analysis (TGA) was performed to investigate carbon deposition on the catalyst (Fig. S37). The spent catalyst collected after the 1000 h-on-stream reaction showed only a 0.4 wt% weight loss compared with the reduced catalyst, indicating that negligible carbon deposition occurred during CO_2 hydrogenation. The 23.5% weight gain observed in the spent catalyst was caused by the oxidation of metallic phases. In addition, temperature-programmed oxidation (TPO) coupled with QMS of the spent Na–CuCo-9 catalyst (1000 h) demonstrated negligible CO_2 formation (Fig. S38). The brown color of the reduced catalyst persisted in the spent catalyst (1000 h), indicating negligible carbon deposition (Fig. S39). The Co-decorated dendritic Cu structure with channels between Cu domains observed after the 200 h-on-stream reaction was maintained in the spent catalyst collected after the 1000 h-on-stream reaction (Fig. S40). The ability of the Na-CuCo-9 catalyst to maintain its high activity by suppressing reoxidation and carbon deposition can be attributed to the continuous interconversion between Cu^0 and $Cu_2^{(1+)}O$ by an oscillatory redox cycle [50]. This helps prevent the formation of stable and inactive Cu oxides, and the suppression of the chain growth reaction, which prevents the excess deposition of carbonaceous species and blockage of active sites.

To date, most efforts to produce alcohols from the direct hydrogenation of CO_2 have focused on methanol and ethanol, wherein producing a significant quantity of C_{3+} alcohols has been a great challenge (Table S1). In this study, we present a single tandem catalyst that is capable of converting oxygenated C_1 and C_2 intermediates to C_{3+} alcohols in a single CO_2 hydrogenation run. The conversion of CH_3O^* and CH_3CHO^* intermediates to CH_3OH and CH_3CHOH, respectively, was highly suppressed over the Na–CoCu-9 catalyst, whereas the production of $C_{3+}OH$ containing an unusually high *n*-butanol fraction was strongly promoted. The production of $C_{3+}OH$ was influenced by the catalyst composition and process conditions. For example, higher temperatures and H_2/CO_2 ratios were detrimental to the formation of $C_{3+}OH$. Following the restructuring of the catalyst morphology during the initial reaction period, the Co-decorated Cu surface remained highly stable during subsequent CO_2 hydrogenation.

In general, methanol synthesis coupled with FTS produces higher alcohols according to the ASF distribution [20]. Thus, the unprecedentedly high selectivity of our catalyst toward *n*-butanol, the production of which was well beyond that predicted by the ASF distribution, should be explained by a new mechanism. A plausible mechanism for the formation of *n*-butanol is shown in Fig. 9. Although the RWGS mechanism over CuCo-based surfaces remains unclear, the presence of Cu^0 and O_v in the NAP-XPS profiles suggests that H_2-assisted CO_2 dissociation could be the main RWGS pathway over the Na–CuCo-9 catalyst [71,72]. A strong balance between dissociated and non-dissociated C–O bonds is essential to encourage $C_{3+}OH$ formation activity, leading to kinetically favorable $C_{3+}OH$ production. The produced CO can be transformed in parallel with CH_3O^* and CH_3 * on the Cu and Co sites, respectively, owing to their distinct intrinsic activities. CH_3 * interacts with *CO to produce a C_{2+} oxygenate intermediate, which is eventually converted to acetaldehyde via hydrogenation [68,70]. The termination of $^*CH_x$ to CH_4 over the Co surface, which competes with the essential insertion of CO* to generate the aldehydic intermediate for *n*-butanol formation, is difficult. Subsequently, the acetaldehyde intermediate is re-adsorbed and activated as $CH_3CHOH^* + CH_2CHO^*$ on the Cu surface. The facilitated C–O bond dissociation of CH_3CHOH^* over the Co site produced CH_3CH^* , with the subsequent C–C coupling reaction between CH_3CH^* and CH_2CHO^* producing C_4 oxygenates as a precursor for the formation of *n*-butanol in a tandem reaction. Therefore, the formation of *n*-butanol is highly dependent on the kinetic rates of several crucial elementary steps, including C–C coupling, C–O dissociation, and C–H formation. Experimental and computational analyses revealed that high *n*-butanol production deviating from the ASF distribution on the Co–Cu catalyst was realized for the first time via the CO_2 → acetaldehyde → *n*-butanol route during CO_2 hydrogenation. The exceptional activity and robust stability of the Na–CuCo-9 catalyst demonstrate its considerable promise in practical applications.

4. Conclusion

In summary, we demonstrated the direct and selective production of *n*-butanol-rich C_{3+} alcohols deviating from the ASF distribution via CO_2 hydrogenation over a bimetallic Co–Cu tandem catalyst. Rigorous experimental tuning revealed that the Na-promoted Cu–Co catalyst with Cu/Co + Cu] = 9 could actively produce $C_{3+}OH$ having a high STY_{C3+OH} of 80.8 mg g^{-1} h^{-1}. The initial restructuring of the catalyst morphology during the initial period of CO_2 hydrogenation led to the migration of Co nanoparticles to the outermost surface of the dendritic Cu substrate; this structure was maintained over a long-term reaction of up to 1000 h. In addition, the suppression of coke formation and

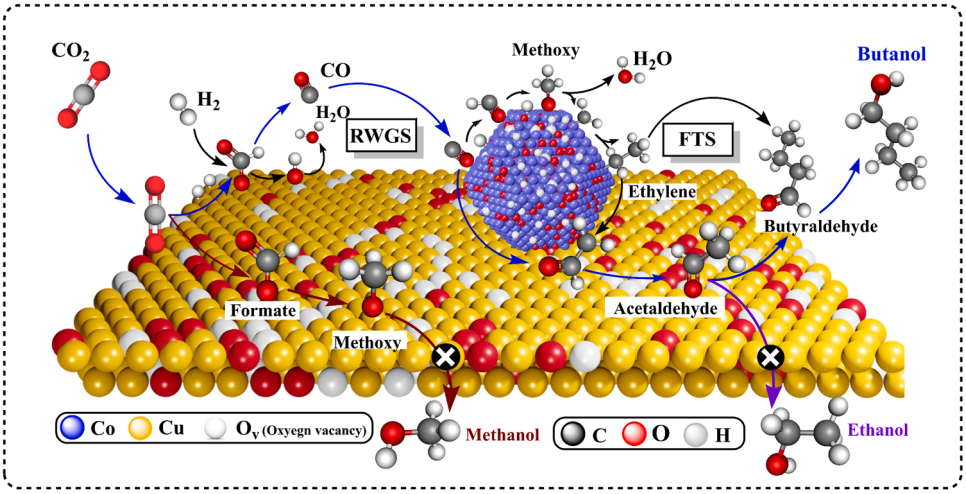

Fig. 9. Schematic of a plausible reaction mechanism and intermediates for the synthesis of *n*-butanol from CO_2 hydrogenation over the Na–CuCo-9 catalyst.

reoxidation during CO_2 hydrogenation led to negligible losses in catalyst activity in terms of CO_2 conversion and $C_{3+}OH$ selectivity. Based on in situ analyses and DFT simulations of various possible routes, the mechanism behind *n*-butanol formation over the catalyst was elucidated as follows: First, the CO produced by rapid RWGS on the Cu site was acquired by the Co site to form CH_x * by C–O dissociation and establish the FTS regime. The insertion of CO into the CH_x * intermediate produced acetaldehyde, which served as an intermediate for *n*-butanol synthesis by C–O dissociation and subsequent C–C coupling. The simple preparation method, high STY_{C3+OH}, and exceptional long-term stability of the Na-promoted Cu–Co catalyst render it a highly promising material in the production of $C_{3+}OH$ under industrially relevant conditions. A further improvement of the catalyst for more selective *n*-butanol synthesis from direct CO_2 conversion can contribute to realize sustainable and carbon-neutral economy.

CRediT authorship contribution statement

Muhammad Irshad: Conceptualization, Methodology, Formal analysis, Data curation, and Writing – original draft. **Hee-Joon Chun:** Methodology, Formal analysis, Investigation, and Writing – original draft. **Muhammad Kashif Khan:** Conceptualization, Methodology, and Investigation. **Heuntae Jo:** Validation and Visualization. **Seok Ki Kim:** Resources, Formal analysis, Investigation, and Writing – review & editing. **Jaehoon Kim:** Supervision, Project administration, Resources, Writing – review & editing, and Funding acquisition.

Declaration of Competing Interest

The authors declare that they have no known competing financial interests or personal relationships that could have appeared to influence the work reported in this paper.

Data availability

Data will be made available on request.

Acknowledgments

This study received funding from the Korea Institute of Energy Technology Evaluation and Planning (KETEP) under the Ministry of Trade, Industry & Energy, Republic of Korea (No. 20224C10300010) and a National Research Council of Science & Technology (NST) grant from the Korean government (MSIT) (No. CAP21012–100). Some experiments were performed at the 8 C and 8A2 synchrotron beamlines of the Pohang Accelerator Laboratory (PAL, Republic of Korea) under Contract Nos. 2023–1st-8 C-032 and 2021–3rd-8A2–002, respectively.

Appendix A. Supporting information

Supplementary data associated with this article can be found in the online version at doi:10.1016/j.apcatb.2023.123201.

References

[1] S. Solomon, G.K. Plattner, R. Knutti, P. Friedlingstein, Irreversible climate change due to carbon dioxide emissions, Proc. Natl. Acad. Sci. USA 106 (2009) 1704–1713, https://doi.org/10.1073/pnas.0812721106.
[2] F.H. Kong, G. Rim, M. Song, C. Rosu, P. Priyadarshini, R.P. Lively, M.J. Realff, C. W. Jones, Research needs targeting direct air capture of carbon dioxide: Material & process performance characteristics under realistic environmental conditions, Korean J. Chem. Eng. 39 (2022) 1–19, https://doi.org/10.1007/s11814-021-0976-0.
[3] C. Hepburn, E. Adlen, J. Beddington, E.A. Carter, S. Fuss, N. Mac Dowell, J.C. Minx, P. Smith, C.K. Williams, The technological and economic prospects for CO_2 utilization and removal, Nature 575 (2019) 87–97, https://doi.org/10.1038/s41586-019-1681-6.
[4] H. Jo, M.K. Khan, M. Irshad, M.W. Arshad, S.K. Kim, J. Kim, Unraveling the role of cobalt in the direct conversion of CO_2 to high-yield liquid fuels and lube base oil, Appl. Catal. B 305 (2022) 121041–121055, https://doi.org/10.1016/j.apcatb.2021.121041.
[5] P. Gao, S. Li, X. Bu, S. Dang, Z. Liu, H. Wang, L. Zhong, M. Qiu, C. Yang, J. Cai, W. Wei, Y. Sun, Direct conversion of CO_2 into liquid fuels with high selectivity over a bifunctional catalyst, Nat. Chem. 9 (2017) 1019–1024, https://doi.org/10.1038/nchem.2794.
[6] D. Goud, R. Gupta, R. Maligal-Ganesh, S.C. Peter, Review of catalyst design and mechanistic studies for the production of olefins from anthropogenic CO_2, ACS Catal. 10 (2020) 14258–14282, https://doi.org/10.1021/acscatal.0c03799.
[7] M.K. Khan, P. Butolia, H. Jo, M. Irshad, D. Han, K.-W. Nam, J. Kim, Selective conversion of carbon dioxide into liquid hydrocarbons and long-chain α-olefins over Fe-amorphous AlO_x bifunctional catalysts, ACS Catal. 10 (2020) 10325–10338, https://doi.org/10.1021/acscatal.0c02611.
[8] M.G. Sibi, M.K. Khan, D. Verma, W. Yoon, J. Kim, High-yield synthesis of BTEX over Na–FeAlOx/Zn–HZSM-5@ SiO_2 by direct CO_2 conversion and identification of surface intermediates, Appl. Catal. B 301 (2022) 120813–120827, https://doi.org/10.1016/j.apcatb.2021.120813.
[9] M.G. Sibi, D. Verma, H.C. Setiyadi, M.K. Khan, N. Karanwal, S.K. Kwak, K. Y. Chung, J.H. Park, D. Han, K.W. Nam, J. Kim, Synthesis of monocarboxylic acids via direct CO_2 conversion over Ni-Zn intermetallic catalysts, ACS Catal. 11 (2021) 8382–8398, https://doi.org/10.1021/acscatal.1c00747.
[10] F. Zeng, C. Mebrahtu, X.Y. Xi, L.F. Liao, J. Ren, J.X. Xie, H.J. Heeres, R. Palkovits, Catalysts design for higher alcohols synthesis by CO_2 hydrogenation: Trends and future perspectives, 120073–112101, Appl. Catal. B 291 (2021), https://doi.org/10.1016/j.apcatb.2021.120073.
[11] D. Xu, Y. Wang, M. Ding, X. Hong, G. Liu, S.C.E. Tsang, Advances in higher alcohol synthesis from CO_2 hydrogenation, Chem (2020) 849–881, https://doi.org/10.1016/j.chempr.2020.10.019.
[12] W.R. da Silva Trindade, R.G. dos Santos, Review on the characteristics of butanol, its production and use as fuel in internal combustion engines, Ren. Sustain. Energy Rev. 69 (2017) 642–651, https://doi.org/10.1016/j.rser.2016.11.213.
[13] J. Klabunde, C. Bischoff, A. Papa, Ullmann's Encycl. Ind. Chem., Wiley, 2018.
[14] H. Hahn, G. Dämbkes, N. Rupprich, H. Bahl, G. Frey, Ullmann's Encycl, Ind. Chem (2013) 1–13.
[15] T. Walther, J.M. Francois, Microbial production of propanol, Biotechnol. Adv. 34 (2016) 984–996, https://doi.org/10.1016/j.biotechadv.2016.05.011.
[16] Y. Nakagawa, N. Tajima, K. Hirao, A theoretical study of catalytic hydration reactions of ethylene, J. Comput. Chem. 21 (2000) 1292–1304, https://doi.org/10.1002/1096-987X(20001115)21:14.
[17] X. Jiang, X. Nie, X. Guo, C. Song, J.G. Chen, Recent advances in carbon dioxide hydrogenation to methanol via heterogeneous catalysis, Chem. Rev. 120 (2020) 7984–8034, https://doi.org/10.1021/acs.chemrev.9b00723.
[18] X.Z. Lim, How to make the most of carbon dioxide, Nature 526 (2015) 628–630, https://doi.org/10.1038/526628a.
[19] W. Zhou, K. Cheng, J. Kang, C. Zhou, V. Subramanian, Q. Zhang, Y. Wang, New horizon in C1 chemistry: breaking the selectivity limitation in transformation of syngas and hydrogenation of CO_2 into hydrocarbon chemicals and fuels, Chem. Soc. Rev. 48 (2019) 3193–3228, https://doi.org/10.1039/C8CS00502H.
[20] H.T. Luk, C. Mondelli, D.C. Ferre, J.A. Stewart, J. Perez-Ramirez, Status and prospects in higher alcohols synthesis from syngas, Chem. Soc. Rev. 46 (2017) 1358–1426, https://doi.org/10.1039/c6cs00324a.
[21] R.P. Ye, J. Ding, W. Gong, M.D. Argyle, Q. Zhong, Y. Wang, C.K. Russell, Z. Xu, A. G. Russell, Q. Li, M. Fan, Y.G. Yao, CO_2 hydrogenation to high-value products via heterogeneous catalysis, Nat. Commun. 10 (2019) 5698–5713, https://doi.org/10.1038/s41467-019-13638-9.
[22] Z. He, Q. Qian, J. Ma, Q. Meng, H. Zhou, J. Song, Z. Liu, B. Han, Water-enhanced synthesis of higher alcohols from CO_2 hydrogenation over a Pt/Co_3O_4 catalyst under milder conditions, Angew. Chem. Int. Ed. 55 (2016) 737–741, https://doi.org/10.1002/anie.201507585.
[23] C. Yang, R. Mu, G. Wang, J. Song, H. Tian, Z.J. Zhao, J. Gong, Hydroxyl-mediated ethanol selectivity of CO_2 hydrogenation, Chem. Sci. 10 (2019) 3161–3167, https://doi.org/10.1039/c8sc05608k.
[24] A.Y. Khodakov, W. Chu, P. Fongarland, Advances in the development of novel cobalt Fischer-Tropsch catalysts for synthesis of long-chain hydrocarbons and clean fuels, Chem. Rev. 107 (2007) 1692–1744, https://doi.org/10.1021/cr050972v.
[25] J. Gong, H. Yue, Y. Zhao, S. Zhao, L. Zhao, J. Lv, S. Wang, X. Ma, Synthesis of ethanol via syngas on Cu/SiO_2 catalysts with balanced Cu^0-Cu^+ sites, J. Am. Chem. Soc. 134 (2012) 13922–13927, https://doi.org/10.1021/ja3034153.
[26] R.F. Susanti, L.W. Dianningrum, T. Yum, Y. Kim, B.G. Lee, J. Kim, High-yield hydrogen production from glucose by supercritical water gasification without added catalyst, Int. J. Hydrog. Energy 37 (2012) 11677–11690, https://doi.org/10.1016/j.ijhydene.2012.05.087.
[27] M.K. Khan, R. Insyani, J. Lee, M. Yi, J.W. Lee, J. Kim, A non-catalytic, supercritical methanol route for effective deacidification of naphthenic acids, Fuel 182 (2016) 650–659, https://doi.org/10.1016/j.fuel.2016.06.023.
[28] B. Ravel, M. Newville, ATHENA, ARTEMIS, HEPHAESTUS: data analysis for X-ray absorption spectroscopy using IFEFFIT, J. Synchrotron Radiat. 12 (2005) 537–541, https://doi.org/10.1107/S0909049505012719.
[29] G. Kim, Y. Yu, H. Lim, B. Jeong, J. Lee, J. Baik, B.S. Mun, K.J. Kim, AP-XPS beamline, a platform for operando science at Pohang Accelerator Laboratory, J. Synchrot. Rad. 27 (2020) 507–514, https://doi.org/10.1107/S160057751901676x.
[30] G. Kresse, J. Hafner, Ab initio molecular dynamics for liquid metals, Phys. Rev. B. Condens. Matter 47 (1993) 558–561, https://doi.org/10.1103/physrevb.47.558.

[31] G. Kresse, J. Hafner, Ab initio molecular-dynamics simulation of the liquid-metal-amorphous-semiconductor transition in germanium, Phys. Rev. B Condens. Matter 49 (1994) 14251–14269, https://doi.org/10.1103/physrevb.49.14251.

[32] G. Kresse, J. Furthmuller, Efficiency of ab-initio total energy calculations for metals and semiconductors using a plane-wave basis set, Comput. Mat. Sci. 6 (1996) 15–50, https://doi.org/10.1016/0927-0256(96)00008-0.

[33] R.B. Rankin, J. Greeley, Trends in selective hydrogen peroxide production on transition metal surfaces from first principles, ACS Catal. 2 (2012) 2664–2672, https://doi.org/10.1021/cs3003337.

[34] R.G. Zhang, F. Liu, B.J. Wang, Co-decorated Cu alloy catalyst for C-2 oxygenate and ethanol formation from syngas on Cu-based catalyst: insight into the role of Co and Cu as well as the improved selectivity, Catal. Sci. Technol. 6 (2016) 8036–8054, https://doi.org/10.1039/c6cy01239f.

[35] M.W. Chase Jr, JANAF thermochemical tables, J. Phys. Chem. Ref. Data (1985).

[36] Y.A. Zhu, D. Chen, X.G. Zhou, W.K. Yuan, DFT studies of dry reforming of methane on Ni catalyst, Catal. Today 148 (2009) 260–267, https://doi.org/10.1016/j.cattod.2009.08.022.

[37] I. Kasatkin, P. Kurr, B. Kniep, A. Trunschke, R. Schlogl, Role of lattice strain and defects in copper particles on the activity of Cu/ZnO/Al_2O_3 catalysts for methanol synthesis, Angew. Chem. Int. Ed. 46 (2007) 7324–7327, https://doi.org/10.1002/anie.200702600.

[38] R.G. Kurniawan, N. Karanwal, J. Park, D. Verma, S.K. Kwak, S.K. Kim, J. Kim, Direct conversion of furfural to 1,5-pentanediol over a nickel-cobalt oxide-alumina trimetallic catalyst, Appl. Catal. B 320 (2023) 121971–121988, https://doi.org/10.1016/j.apcatb.2022.121971.

[39] L.S. Kau, D.J. Spira-Solomon, J.E. Penner-Hahn, K.O. Hodgson, E.I. Solomon, X-ray absorption edge determination of the oxidation state and coordination number of copper. Application to the type 3 site in Rhus vernicifera laccase and its reaction with oxygen, J. Am. Chem. Soc. 109 (1987) 6433–6442, https://doi.org/10.1021/ja00255a032.

[40] Z. Xiao, Y. Wang, Y.-C. Huang, Z. Wei, C.-L. Dong, J. Ma, S. Shen, Y. Li, S. Wang, Filling the oxygen vacancies in Co_3O_4 with phosphorus: an ultra-efficient electrocatalyst for overall water splitting, Energy Environ. Sci. 10 (2017) 2563–2569, https://doi.org/10.1039/C7EE01917C.

[41] H.C. Choi, S.Y. Lee, S.B. Kim, M.G. Kim, M.K. Lee, H.J. Shin, J.S. Lee, Local structural characterization for electrochemical insertion-extraction of lithium into CoO with X-ray absorption spectroscopy, J. Phys. Chem. B 106 (2002) 9252–9260, https://doi.org/10.1021/jp0205968.

[42] M.C. Biesinger, Advanced analysis of copper X-ray photoelectron spectra, Surf. Interf. Anal. 49 (2017) 1325–1334, https://doi.org/10.1002/sia.6239.

[43] J. Chastain, R.C. King Jr, Handbook of X-ray photoelectron spectroscopy, Perkin Elmer Corp. 40 (1992) 221.

[44] M.C. Biesinger, B.P. Payne, A.P. Grosvenor, L.W.M. Lau, A.R. Gerson, R.S. Smart, Resolving surface chemical states in XPS analysis of first row transition metals, oxides and hydroxides: Cr, Mn, Fe, Co and Ni, Appl. Surf. Sci. 257 (2011) 2717–2730, https://doi.org/10.1016/j.apsusc.2010.10.051.

[45] T. Chuang, C. Brundle, D. Rice, Interpretation of the X-Ray photoemission spectra of cobalt oxides and cobalt oxide surfaces, Surf. Sci. 59 (1976) 413–429, https://doi.org/10.1016/0039-6028(76)90026-1.

[46] Q. Guo, S.G. Xia, X.B. Li, Y. Wang, F. Liang, Z.S. Lin, C.H. Tung, L.Z. Wu, Flower-like cobalt carbide for efficient carbon dioxide conversion, Chem. Commun. 56 (2020) 7849–7852, https://doi.org/10.1039/d0cc01091j.

[47] M. Favaro, H. Xiao, T. Cheng, W.A. Goddard 3rd, J. Yano, E.J. Crumlin, Subsurface oxide plays a critical role in CO_2 activation by Cu(111) surfaces to form chemisorbed CO_2, the first step in reduction of CO_2, Proc. Natl. Acad. Sci. USA 114 (2017) 6706–6711, https://doi.org/10.1073/pnas.1701405114.

[48] S. Liu, C. Yang, S. Zha, D. Sharapa, F. Studt, Z.J. Zhao, J. Gong, Moderate surface segregation promotes selective ethanol production in CO_2 hydrogenation reaction over CoCu catalysts, Angew. Chem. Int. Ed. Engl. 61 (2022) e202109027–e202109032, https://doi.org/10.1002/anie.202109027.

[49] F. Yang, Y. Choi, P. Liu, J. Hrbek, J.A. Rodriguez, inducecatalytic reduction of a Cu_2O/Cu (111) surface by CO: STM, XPS, and DFT studies, J. Phys. Chem. C. 114 (2010) 17042–17050, https://doi.org/10.1021/jp1029079.

[50] J. Cao, A. Rinaldi, M. Plodinec, X. Huang, E. Willinger, A. Hammud, S. Hieke, S. Beeg, L. Gregoratti, C. Colbea, R. Schlogl, M. Antonietti, M. Greiner, M. Willinger, In situ observation of oscillatory redox dynamics of copper, Nat. Commun. 11 (2020) 3554–3565, https://doi.org/10.1038/s41467-020-17346-7.

[51] T. Koitaya, S. Yamamoto, Y. Shiozawa, Y. Yoshikura, M. Hasegawa, J.Y. Tang, K. Takeuchi, K. Mukai, S. Yoshimoto, I. Matsuda, J. Yoshinobu, CO_2 activation and reaction on Zn-deposited Cu surfaces studied by ambient-pressure X-ray photoelectron spectroscopy, ACS Catal. 9 (2019) 4539–4550, https://doi.org/10.1021/acscatal.9b00041.

[52] S. Kattel, P.J. Ramírez, J.G. Chen, J.A. Rodriguez, P. Liu, Active sites for CO_2 hydrogenation to methanol on Cu/ZnO catalysts, Science 355 (2017) 1296–1299, https://doi.org/10.1126/science.aal3573.

[53] S. Kattel, P. Liu, J.G.G. Chen, Tuning selectivity of CO_2 hydrogenation reactions at the metal/oxide interface, J. Am. Chem. Soc. 139 (2017) 9739–9754, https://doi.org/10.1021/jacs.7b05362.

[54] C.S. Yang, S.H. Liu, Y.N. Wang, J.M. Song, G.S. Wang, S. Wang, Z.J. Zhao, R.T. Mu, J.L. Gong, The interplay between structure and product selectivity of CO_2 hydrogenation, Angew. Chem. Int. Ed. 58 (2019) 11242–11247, https://doi.org/10.1002/anie.201904649.

[55] K. Mudiyanselage, S.D. Senanayake, L. Feria, S. Kundu, A.E. Baber, J. Graciani, A. B. Vidal, S. Agnoli, J. Evans, R. Chang, S. Axnanda, Z. Liu, J.F. Sanz, P. Liu, J. A. Rodriguez, D.J. Stacchiola, Importance of the metal-oxide interface in catalysis: in situ studies of the water-gas shift reaction by ambient-pressure X-ray photoelectron spectroscopy, Angew. Chem. Int. Ed. Engl. 52 (2013) 5101–5105, https://doi.org/10.1002/anie.201210077.

[56] T. Lin, X. Qi, X. Wang, L. Xia, C. Wang, F. Yu, H. Wang, S. Li, L. Zhong, Y. Sun, Direct production of higher oxygenates by syngas conversion over a multifunctional catalyst, Angew. Chem. Int. Ed. 58 (2019) 4627–4631, https://doi.org/10.1002/anie.201814611.

[57] D. Xu, M. Ding, X. Hong, G. Liu, S.C.E. Tsang, Selective C_{2+} alcohol synthesis from direct CO_2 hydrogenation over a Cs-promoted Cu-Fe-Zn catalyst, ACS Catal. 10 (2020) 5250–5260, https://doi.org/10.1021/acscatal.0c01184.

[58] M. Behrens, F. Studt, I. Kasatkin, S. Kuhl, M. Havecker, F. Abild-Pedersen, S. Zander, F. Girgsdies, P. Kurr, B.L. Kniep, M. Tovar, R.W. Fischer, J.K. Norskov, R. Schlogl, The active site of methanol synthesis over Cu/ZnO/Al_2O_3 industrial catalysts, Science 336 (2012) 893–897, https://doi.org/10.1126/science.1219831.

[59] A. Parastaev, V. Muravev, E.H. Osta, T.F. Kimpel, J.F.M. Simons, A.J.F. van Hoof, E. Uslamin, L. Zhang, J.J.C. Struijs, D.B. Burueva, E.V. Pokochueva, K.V. Kovtunov, I.V. Koptyug, I.J. Villar-Garcia, C. Escudero, T. Altantzis, P. Liu, A. Beche, S. Bals, N. Kosinov, E.J.M. Hensen, Breaking structure sensitivity in CO_2 hydrogenation by tuning metal-oxide interfaces in supported cobalt nanoparticles, Nat. Catal. 5 (2022) 1051–1060, https://doi.org/10.1038/s41929-022-00874-4.

[60] S.M. Fehr, I. Krossing, Spectroscopic signatures of pressurized carbon dioxide in diffuse reflectance infrared spectroscopy of heterogeneous catalysts, ChemCatChem 12 (2020) 2622–2629, https://doi.org/10.1002/cctc.201902038.

[61] D. Coker, J. Reimers, R. Watts, The infrared absorption spectrum of water, Aust. J. Phy. 35 (1982) 623–638, https://doi.org/10.1071/PH820623.

[62] F. Morales, E. de Smit, F.M. de Groot, T. Visser, B.M. Weckhuysen, Effects of manganese oxide promoter on the CO and H_2 adsorption properties of titania-supported cobalt Fischer–Tropsch catalysts, J. Catal. 246 (2007) 91–99, https://doi.org/10.1016/j.jcat.2006.11.014.

[63] T. Das, G. Deo, Synthesis, characterization and in situ DRIFTS during the CO_2 hydrogenation reaction over supported cobalt catalysts, J. Mol. Catal. A: Chem. 350 (2011) 75–82, https://doi.org/10.1016/j.molcata.2011.09.008.

[64] Y. Yang, C.A. Mims, R.S. Disselkamp, J.H. Kwak, C.H.F. Peden, C.T. Campbell, Non)formation of methanol by direct hydrogenation of formate on copper catalysts, J. Phys. Chem. C. 114 (2010) 17205–17211, https://doi.org/10.1021/jp104068k.

[65] L. Wang, L. Wang, J. Zhang, X. Liu, H. Wang, W. Zhang, Q. Yang, J. Ma, X. Dong, S. J. Yoo, J.G. Kim, X. Meng, F.S. Xiao, Selective hydrogenation of CO_2 to ethanol over cobalt catalysts, Angew. Chem. Int. Ed. 57 (2018) 6104–6108, https://doi.org/10.1002/anie.201800729.

[66] J. Graciani, K. Mudiyanselage, F. Xu, A.E. Baber, J. Evans, S.D. Senanayake, D. J. Stacchiola, P. Liu, J. Hrbek, J. Fernandez Sanz, J.A. Rodriguez, Catalysis. Highly active copper-ceria and copper-ceria-titania catalysts for methanol synthesis from CO_2, Science 345 (2014) 546–550, https://doi.org/10.1126/science.1253057.

[67] M.H. Zhang, R. Yao, H.X. Jiang, G.M. Li, Y.F. Chen, Insights into the mechanism of acetic acid hydrogenation to ethanol on Cu(111) surface, Appl. Surf. Sci. 412 (2017) 342–349, https://doi.org/10.1016/j.apsusc.2017.03.222.

[68] L.P. Ding, T.T. Shi, J. Gu, Y. Cui, Z.Y. Zhang, C.J. Yang, T. Chen, M. Lin, P. Wang, N.H. Xue, L.M. Peng, X.F. Guo, Y. Zhu, Z.X. Chen, W.P. Ding, CO_2 hydrogenation to ethanol over Cu@Na-beta, Chem 6 (2020) 2673–2689, https://doi.org/10.1016/j.chempr.2020.07.001.

[69] C. Li, Y. Zhang, D. Li, B. Wang, C.K. Russell, M. Fan, R. Zhang, The newly-assisted catalytic mechanism of surface hydroxyl species performed as the promoter in syngas-to-C_2 species on the Cu-based bimetallic catalysts, Green. Energy Environ. (2021) 487–498, https://doi.org/10.1016/j.gee.2021.06.001.

[70] L.R.L. Ting, R. Garcia-Muelas, A.J. Martin, F.L.P. Veenstra, S.T. Chen, Y. Peng, E.Y. X. Per, S. Pablo-Garcia, N. Lopez, J. Perez-Ramirez, B.S. Yeo, Electrochemical reduction of carbon dioxide to 1-butanol on oxide-derived copper, Angew. Chem. Int. Ed. 59 (2020) 21072–21079, https://doi.org/10.1002/anie.202008289.

[71] M. Behrens, F. Studt, I. Kasatkin, S. Kuhl, M. Havecker, F. Abild-Pedersen, S. Zander, F. Girgsdies, P. Kurr, B.L. Kniep, M. Tovar, R.W. Fischer, J.K. Norskov, R. Schlogl, The active site of methanol synthesis over Cu/ZnO/Al_2O_3 industrial catalysts, Science 336 (2012) 893–899, https://doi.org/10.1126/science.1219831.

[72] H.X. Liu, S.Q. Li, W.W. Wang, W.Z. Yu, W.J. Zhang, C. Ma, C.J. Jia, Partially sintered copper-ceria as excellent catalyst for the high-temperature reverse water gas shift reaction, Nat. Commun. 13 (2022) 867–877, https://doi.org/10.1038/s41467-022-28476-5.

[73] W. Guo, W.G. Gao, H. Wang, J.J. Tian, Higher alcohols synthesis from CO_2 hydrogenation over K_2O-modified CuZnFeZrO$_2$ catalysts, Adv. Mat. Res 827 (2014) 20–24, https://doi.org/10.4028/www.scientific.net/AMR.827.20.

[74] S. Liu, H.B. Zhou, L. Zhang, Z. Ma, Y.D. Wang, Activated carbon-supported Mo-Co-K sulfide catalysts for synthesizing higher alcohols from CO_2, Chem. Eng. Technol. 42 (2019) 962–970, https://doi.org/10.1002/ceat.201800401.

[75] S. Liu, H.B. Zhou, Q.Y. Song, Z. Ma, Synthesis of higher alcohols from CO_2 hydrogenation over Mo-Co-K sulfide-based catalysts, J. Taiwan Chem. Eng. 76 (2017) 18–26, https://doi.org/10.1016/j.jtice.2017.04.007.

[76] B. Ouyang, S.H. Xiong, Y.H. Zhang, B. Liu, J.L. Li, The study of morphology effect of Pt/Co_3O_4 catalysts for higher alcohol synthesis from CO_2 hydrogenation, Appl. Catal. A: Gen. 543 (2017) 189–195, https://doi.org/10.1016/j.apcata.2017.06.031.

[77] R.W. Yao, J. Wei, Q.J. Ge, J. Xu, Y. Han, Q.X. Ma, H.Y. Xu, J. Sun, Monometallic iron catalysts with synergistic Na and S for higher alcohols synthesis via CO_2

hydrogenation, Appl. Catal. B 298 (2021) 120556–120564, https://doi.org/10.1016/j.apcatb.2021.120556.
[78] D. Xu, H.Q. Yang, X.L. Hong, G.L. Liu, S.C.E. Tsang, Tandem catalysis of direct CO_2 hydrogenation to higher alcohols, ACS Catal. 11 (2021) 8978–8984, https://doi.org/10.1021/acscatal.1c01610.
[79] S.N. Zhang, Z.X. Wu, X.F. Liu, Z.L. Shao, L. Xia, L.S. Zhong, H. Wang, Y.H. Sun, Tuning the interaction between Na and Co_2C to promote selective CO_2 hydrogenation to ethanol, Appl. Catal. B 293 (2021) 120207–120216, https://doi.org/10.1016/j.apcatb.2021.120207.